STUDY ON MICROMECHANICAL FRACTURE MODELS OF STRUCTURAL STEEL AND ITS WELDS

Xi-Yue Liu [1], Yuan-Qing Wang [2], Yi-Du Bu [3, *] and Yang Guan [4]

[1] National University of Defense Technology

[2] Tsinghua University

[3] Beijing University of Technology

[4] Zhuzong Real Estate Development Co., Ltd

*(Corresponding author: E-mail: yidubu@bjut.edu.cn)

ABSTRACT

Steel structures have been widely used in constructions due to their advantages of lightweight, high strength, short construction time and high recycling and reuse potential. Fracture failure in steel structures should be prevented to avoid collapse of the whole structures. Micromechanical fracture models can capture the fracture initiation mechanisms and therefore can be used to predict ductile fractures in steel. Twelve smooth round bars were carried out to obtain the material properties and 36 notched round bars were tested to calibrate the parameters of stress modified critical strain (SMCS) model and the void growth model (VGM) for structural steels (Q235B and Q345B) and the corresponding welds. Specimens were extracted from the base metal, the weld metal and the heat affected zone (HAZ) to investigate fracture behaviour in different parts of the welded joint. Scanning electron microscope (SEM) measurements were taken and finite element models were developed to calibrate the models. The test results and calibrated parameters are reported. Moreover, the calibrated models are applied to analyses the fracture behaviour of welded joints and their accuracy are validated. The calibrated and validated models can be used for further numerical fracture analysis in welded steel structures.

ARTICLE HISTORY

1. Introduction

Fracture failure in steel structures should be prevented to avoid collapse of the whole structures. Structural steel generally exhibits ductile fracture behaviour with significant plasticity. Conventional fracture mechanics, however, assumes pre-existing cracks with high strain constraint, offering better fit for brittle fracture with low plasticity. Moreover, the conventional fracture mechanic methods do not take triaxiality into consideration, thus it is not suitable to predict the fracture for welded steel connections or other welded steel components controlled by triaxial stress condition. Micromechanical facture models assume three stages of microvoid nucleation, void growth, and void coalescence, which capture the effect of stress and strain state on fracture behaviour and can be used in finite element analyses to predict the fracture initiation more accurately.

Earlier models[1] for ductile failure assume homogenous continuum with no stress state. In 1969, Rice and Tracey[2] investigated the influence of triaxial hydrostatic stresses on the process of micromechanical void coalescence analytically, which served as the basis of void growth model (VGM). In 1976, Hancock and Mackenzie[3] carried out tests in different steels to determine the strain required to initiate ductile failure in multi-axial stress-states and proposed that void expansion and coalescence is related to orientation and stress triaxiality. Hancock and Cowling[4] presented the failure mechanisms in three stages: micro void nucleation, growth, and coalescence. Later in 1983, Hancock and Brown[5] conducted experiments and finite deformation stress analysis in a range of structural steels and proposed that the strain to initiate failure is related to the stress state. Similar models have been proposed and tested for various materials by Johnson and Cook[6], Marini et al.[7], Panontin and Sheppard[8] and Bandstra et al.[9]. More recently in 2006, Kanvinde and Deierlein[10] carried out material tests and finite-element analyses for seven varieties of structural steels to validate the material dependent parameters. In 2006, Chi[11] calibrated the toughness parameters of stress modified critical strain model (SMCS) model for mild A572 Grade 50 steel from a series of notched tensile tests. In 2010, Benzerga and Leblond[12] examined the micromechanical models of various stages of ductile fracture and conducted fracture prediction by crack growth simulation. In 2010, Myers et al.[13] conducted 23 uniaxial tensile tests and verified that the sample size was not significantly related to the toughness parameters of the SMCS model. In 2011, Wang et al.[14] compared VGM , SMCS models and J-integral methods in the ductile fracture analysis of welded steel joints and found out that the VGM and SMCS models offered more accurate predictions. In 2012, Kossakowski[15] conducted fracture prediction for S235JR steel using SMCS fracture criterion and concluded that using the characteristic length of the material as mesh size

in finite element analysis offered better accuracy. In 2012, Liao et al.[16] conducted material tests on the base material of Q345 steel, weld deposit metal and heat affected zone, and calibrated the toughness parameters of VGM and SMCS model. Steel joint test data was used to verify the applicability of VGM and SMCS prediction. In 2013, Kiran et al.[17] studied the ductile fracture behaviour of A992 steel under high stress triaxiality, and calibrated the toughness parameters of VGM and SMCS models. In 2015, Liu et al.[18] and Lu[19] calibrated the toughness parameters of VGM model, SMCS model for Q460C high-strength steel and Q235 steel, respectively.

Recent studies have focused on the toughness parameter calibration for different materials. With calibrated material dependent parameters, the micromechanical models can be used in ductile fracture prediction and offer good prediction. Q235B and Q345B are two most commonly used structural steels and previous studies have investigated the parameters separately. In this paper, the ductile fracture behaviour of the base metal, the weld metal and the heat affect zone for these two steels were studied and compared systematically. The micromechanical models of structural steels under monotonic loading were investigated, including the void growth model (VGM) and the stress modified critical strain model (SMCS). Material dependent parameters in the models were calibrated, including the toughness parameters η_{mon} and γ. Scanning electron microscope (SEM) measurements were taken to determine the characteristic length $l*$. Even though Q235B and Q345B are the most commonly used structural steels in China, the calibrations of the above three material dependent parameters for Q235B and Q345B welded steels is scarce. The calibrated micromechanical models can be used for further numerical fracture analysis of different types of welded steel joints and offer more accurate prediction in fractural behaviour.

2. Theory

Previous studies show that fracture initiation is dependent on both the strain state and the stress triaxiality of the material. Micromechanical models can be used to capture the initiation of the cracks and to predict the fracture failure of the component. The models reveal the interaction between stress and strain state and combine micromechanical level void deformation with crack initiation. Two micromechanical models have been considered in this paper and are described below.

2.1. Void growth model (VGM model)

In 1969 Rice and Tracey[2] deduced the analytical solutions in elastic-plastic materials, considering the influence of stress triaxiality and

plastic strain on microvoid expansion of individual cylindrical and spherical void. Expanding on the derivations a critical value η_{mon} is defined to represent the critical state of crack initiation, corresponding to the state of void coalescence. η_{mon} is defined as follow:

$$\eta_{mon} = \frac{\ln\left(\dfrac{R}{R_0}\right)_{critical}}{C} = \int_0^{\varepsilon_p} \exp(1.5T).d\varepsilon_p \tag{1}$$

where R is radius at fracture, R_0 is the initial radius, T is the triaxiality of the stress and $T = \sigma_m/\sigma_e$, σ_m is the mean stress and σ_e is the von Mises stress. η_{mon} is a material dependent parameter which determines the toughness of the material. A larger value of η_{mon} shows better ductility of a material. η_{mon} can be calibrated from notched bar material tests. The fracture criterion of void growth model is expressed as fracture index FI_{VGM}:

$$FI_{VGM} = \int_0^{\varepsilon_p^{critical}} \exp(1.5T)d\varepsilon_p - \eta_{mon} > 0 \tag{2}$$

where $\varepsilon_p^{critical}$ is the equivalent plastic strain at the critical state. $FI_{VGM}=0$ represents the critical state while $FI_{VGM}>0$ indicates the initiation of the fracture.

2.2. Stress modified critical strain (SMCS model)

In VGM, the stress triaxiality is integrated with respect to the material's plastic strain throughout the loading process. In reality the variation of the stress triaxiality throughout the loading process is normally small, therefore the integral term can be substituted with a material dependent constant, as shown in Eq. 3.

$$\ln\left(\frac{R}{R_0}\right)_{monoionic}^{critical} = C\exp\left(\frac{1.5\sigma_m}{\sigma_c}\right).\varepsilon_p^{critical} \tag{3}$$

The critical equivalent plastic strain $\varepsilon_p^{critical}$ and toughness parameter γ can be expressed as follow:

$$\gamma = \frac{\ln\left(\dfrac{R}{R_0}\right)_{monotonic}^{critical}}{C} = \varepsilon_p^{critical}.\exp(1.5T) \tag{4}$$

The fracture criterion of SMCS is expressed as fracture index FI_{SMCS}:

$$FI_{SMCS} = \varepsilon_p - \gamma.\exp(-1.5T) > 0 \tag{5}$$

where SMCS is the fracture criterion. $FI_{SMCS} = 0$ represents the critical state while $FI_{SMCS}>0$ indicates the initiation of the fracture.

The VGM model considers the variation of stress triaxiality during the loading process, offering a more accurate theoretical solution. The SMCS model which assumes that the stress triaxiality does not change with respect to equivalent plastic strain offers a more efficient calculation. It is worth noting that the microstructural void growth and coalescence should also be considered, and failure criterion can only be reached, for both VGM and SMCS, if multiple material points within a certain length scale reach the fracture criterion. This length serves as another parameter, known as characteristic length l^*. l^* is based on the microstructure of the material, thus can be measured by a microscope.

3. Ductile fracture tests

3.1. Material

The materials studied in this paper are two of the most commonly used structural steel materials in China: Q235B and Q345B, with nominal yield strength of 235 MPa and 345 MPa, respectively. All specimens were extracted from 24 mm thick plates. The chemical compositions of the plate material, as provided in the manufacturer's mill certificates, are reported in Tables 1 and 2. Two steel plates of 24 mm were connected with full penetration butt weld as shown in Fig. 1. Welding parameters are listed in Table 3. Specimens from three parts were extracted and investigated: base metal, weld metal and heat affected zone. The relative position of the coupons and the weld is described later.

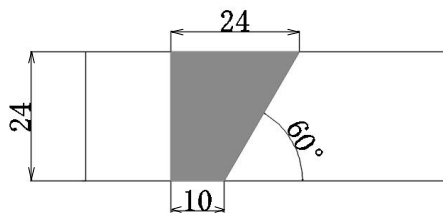**Table 1**
Chemical composition of Q235B steel

Chemical composition quality score /%					
C	Mn	Si	P	S	Ni
≤0.2	0.3~0.7	≤0.35	≤0.045	≤0.045	≤0.80

Table 2
Chemical composition of Q345B steel

Chemical composition quality score /%								
C	Mn	Si	P	S	V	Nb	Ti	Al
≤0.	1.00~1.	≤0.5	≤0.0	≤0.0	0.02~0.	0.015~0.0	0.02~0.	≥0.0

Table 3
Welding Process Parameters

Welding method	Position of welding	Wire model	Wire diameter /mm	Gas	Electric current /A	Voltage /V	Pre-heat temperature/°C	Welding speed /cm/min
Gas shielded welding	Flat welding	E4303/ER50-6	ϕ 1.2	CO_2	260	30	60	20-35

3.2. Smooth round bar tensile tests

3.2.1. Test specimens and test setup

Standard round bar specimens were designed according to the Chinese standard GB/T228.1-2010[20] and extracted from the base metal, the weld metal, and the heat affected zone (HAZ), which is within 10 mm from the edge of the welding seam, as shown in Fig. 2. For each type of coupon two repetitive tests were carried out and the average response were used. The tested coupons are listed in Table 4. The specimens are designated with three letters, with the first two representing the position of the coupon (BM for base metal, WM for weld metal and HM for heat affected zone) and the last letter representing the material of the coupon (L for Q235B and H for Q345B). The geometries of the coupons are presented in Fig. 3. Note that the coupons from HAZ were designed smaller so only material in HAZ was considered.
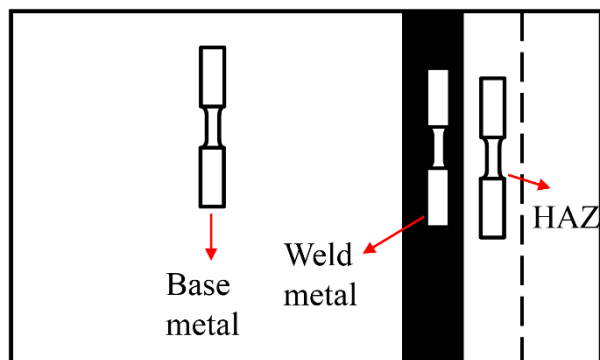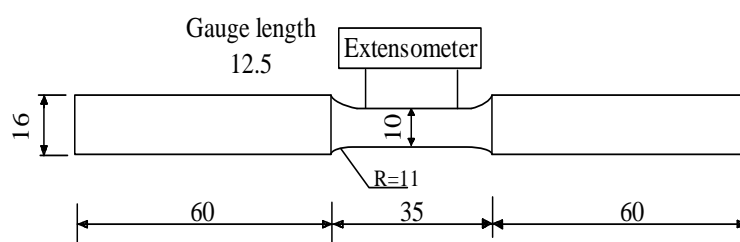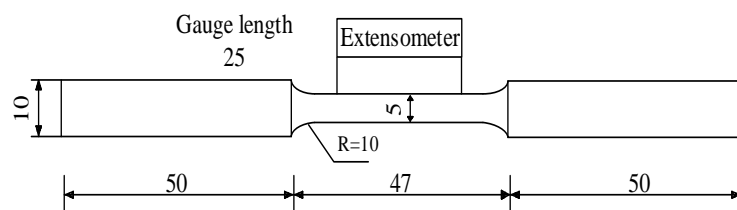

Fig. 1 Schematic drawing of the butt weld (mm)

Fig. 2 Specimens layout

Table 4
List of test coupons

Position	Material	ID	Gauge length (mm)	Quantity
Base metal	Q235B	BML	12.5	2
	Q345B	BMH	12.5	2
Weld metal	Q235B	WML	12.5	2
	Q345B	WMH	12.5	2
Heat affected	Q235B	HML	25.0	2
zone	Q345B	HMH	25.0	2

(a) Dimensions of base metal and weld metal specimens (mm)

(b) Dimensions of HAZ specimens (mm)

Fig. 3 Standard round bar specimen dimensions

The experiments were conducted in the State Key Laboratory of Metal Matrix Composites of Shanghai Jiao Tong University. All tensile tests were conducted using a 100 kN Zwick Roell universal material testing machine, following the procedure set out in the Chinese standard GB/T228.1-2010[20]. A two-stage loading protocol was used to capture the initiation of the fracture, with a loading rate of 0.5 mm/min prior to the yielding point of the material and 1.0 mm/min afterwards. In previous studies, the extensometer is often taken off the specimen after the onset of necking to avoid damage from vibration upon fracture. The extensometer used herein is connected with springs to protect it from the vibration damage caused by the sudden failure of the specimen, thus the whole process can be captured. The gauge length was 12.5 mm. The test loading device and measurement are shown in Fig. 4.

(a) Loading device

(b) Extensometer

Fig. 4 Test setup

3.2.2. Test results

The stress and strain curves obtained during the test are shown in Fig. 5. Only one typical stress-strain curve for each type of the specimens was presented while the obtained mechanical properties were averaged and listed in

Table 5, including the yield strength σ_y, tensile strength σ_u, elastic modulus E, diameter at fracture d_f which was measured by a microscope after the tests, as shown in Fig. 6, fracture load N_f, fracture stress $\sigma_{true,f}$, and the calculated corresponding fracture strain $\varepsilon_{true,f}$.
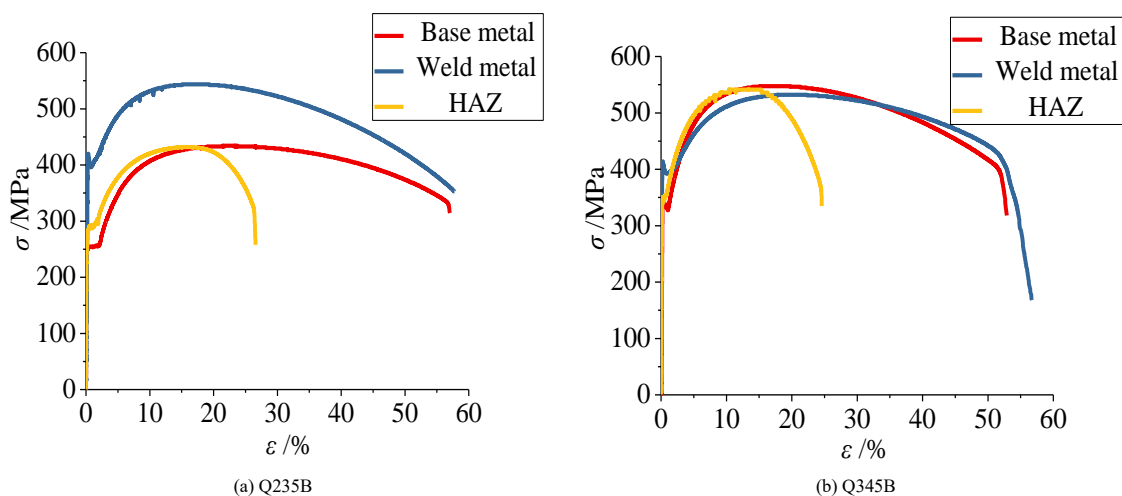

(a) Q235B

(b) Q345B

Fig. 5 Stress-strain curves

Fig. 6 Microscope setup

Table 5
Measured material properties from tensile coupon tests

Material	Position	ID	σ_y/MPa	σ_u/Mpa	E/Mpa	d_f/mm	N_f/kN	$\sigma_{true,f}$/Mpa	$\varepsilon_{true,f}$
Q235B	Base metal	BML-1	258.03	437.96	219164	6.339	25.10	795.42	0.903
		BML-2	253.78	427.16	217251	5.966	26.20	937.19	1.031
		Average	255.91	432.56	218208	6.153	25.65	866.31	0.967
	Weld metal	WML-1	396.64	544.59	208176	5.410	27.70	1205.02	1.227
		WML-2	398.40	547.35	203673	5.407	28.40	1237.08	1.230
		Average	397.52	545.97	205924	5.559	28.05	1159.35	1.170
	HAZ	HML-1	287.58	433.40	115861	3.047	6.36	872.50	1.000
		HML-2	301.10	448.57	114105	3.044	6.48	890.66	0.967
		Average	295.09	437.95	114983	3.058	6.32	860.80	0.976
Q345B	Base metal	BMH-1	346.64	558.30	184330	6.023	31.01	1088.18	0.994
		BMH-2	342.57	560.22	196011	5.991	31.30	1110.38	1.002
		Average	344.61	559.26	190171	6.007	31.15	1099.28	0.998
	Weld metal	WMH-2	390.10	526.10	212135	6.209	31.90	1053.50	0.955
		WMH-3	394.60	535.54	205078	6.340	32.60	1032.74,	0.905
		Average	392.35	530.82	208607	6.275	32.25	1043.12	0.930
	HAZ	HMH-1	353.06	541.30	112120	2.729	7.18	1227.60	1.218
		HMH-2	358.42	559.24	118395	2.928	7.69	1142.67	1.070
		Average	355.74	550.27	115258	2.829	7.44	1185.14	1.144

The measured engineering stress-strain responses were converted into true stress σ_{true} and log plastic strain ε_p using Eqs. 6 and 7,

$$\varepsilon_{true} = \ln(1 + \varepsilon_{eng}) \tag{6}$$

$$\sigma_{true} = \sigma_{eng}(1 + \varepsilon_{eng}) \tag{7}$$

$$\varepsilon_p = \varepsilon_{true} - \frac{\sigma_{true}}{E} \tag{8}$$

where σ_{eng} and ε_{eng} are the engineering stress and strain, respectively while E is the Young's modulus. From the onset of necking during the tensile tests, the elongation was no longer uniform within the gauge length but concentrated in the necking area. Therefore, the stress-strain curves obtained from the tests were used till the onset of necking and extended to the point of fracture, which can be calculated with Eqs. 9 and 10.

$$\sigma_{true,f} = P_f / (\pi d_f^2 / 4) \tag{9}$$

$$\varepsilon_{true,f} = \ln[(d_0 / d_f)^2] \tag{10}$$

where d_f is the fracture diameter and was measured by a microscope, as shown in Fig. 6. The obtained true stress-plastic strain response was extended to fracture and is shown in Fig. 7 and was later input into finite element analyses software in multi-linear form.
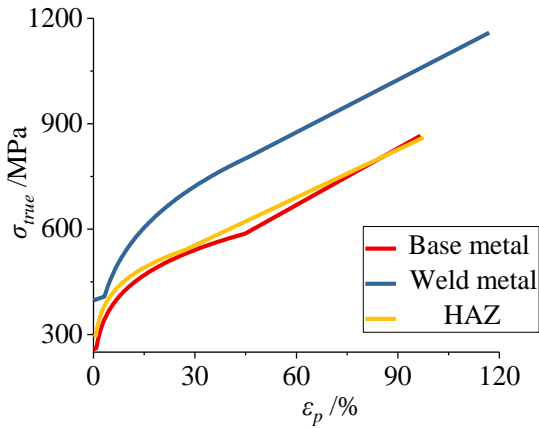
(a) Q235B
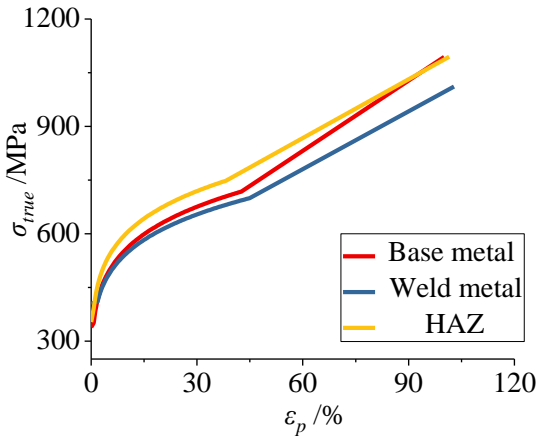
(b) Q345B

Fig. 7 True stress-plastic strain curves

3.2.2. Fracture surface analysis

Scanning electron microscope (SEM) measurements were taken at the Electron Microscopy Scanning Laboratory of School of Materials Science and Technology, Tsinghua University. Scanning electron microscope Quanta FEG 450 was used to observe the crystal shapes and fracture morphologies of all tested samples.
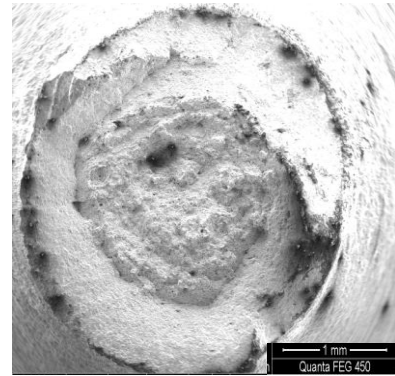
The macroscopic morphology of a typical fracture section is shown in Fig. 8. The fracture surface is composed of three parts: fibre zone, radiation zone, and shear lip zone, which corresponds to crack initiation zone, crack propagation zone, and shear fracture zone[19,21]. The fibre zone is located at the centre of the fracture. The macroscopic morphology of this zone shows a sawtooth fracture surface formed by microscopic voids. The radiation zone shows the rapid and unstable crack propagation. The out edge of the fracture surface is the shear lip zone, where the material fractured under shear force, with a smooth surface. The morphology shows that crack initiated from the centre and propagated through the whole section.
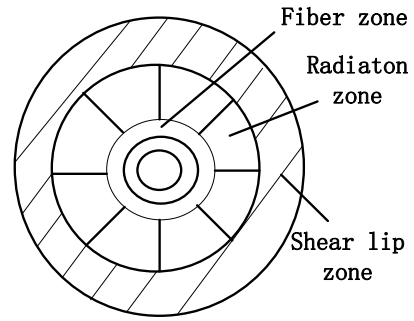
(a) Schematic drawing of the fracture section
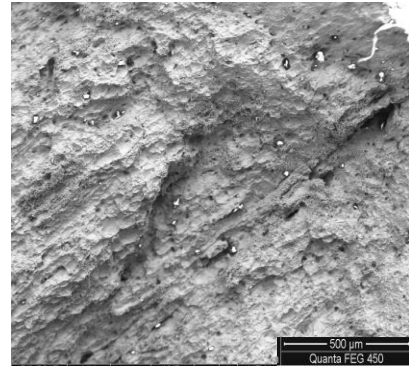
(b) Fibre zone fracture morphology

(c) Fracture section morphology

Fig. 8 Macroscopic fracture morphology

The commonly used structure steel often experiences ductile fracture with high level of plastic deformation. The microscopic morphology of a typical fracture surface is shown in Fig. 9. Dimples with different shapes, sizes, and depths can be observed on the fracture surface. The size and depth of the dimples are related to the stress state and the number of void nucleation. The dimples observed from the centre of fracture surface are mostly large and deep, showing good plasticity of the Q235B and Q345B.
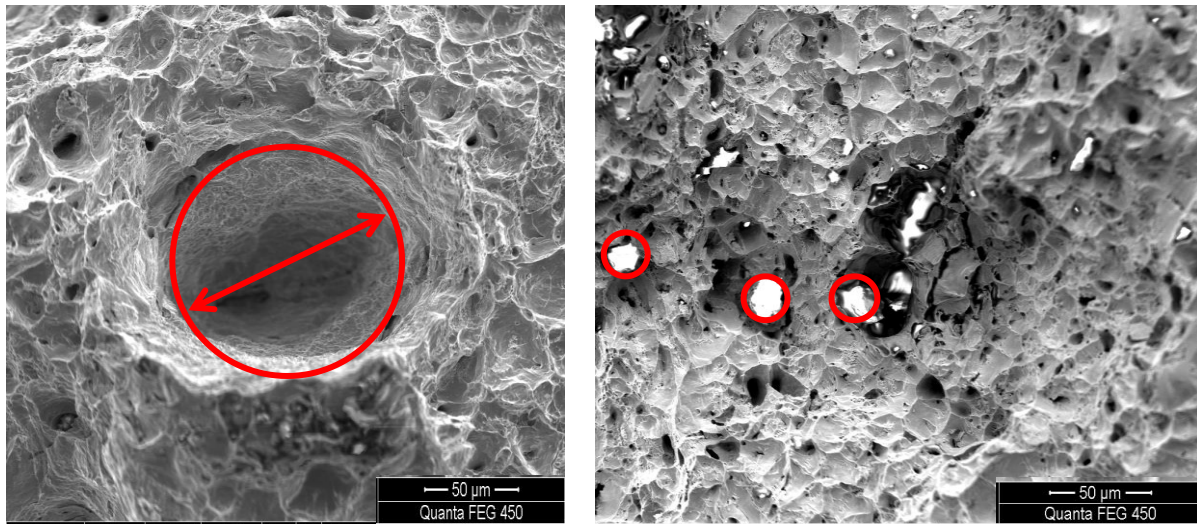
Fig. 9 Scanning electron microscope morphology

3.3. Smooth-notched tensile test (SNTT)

3.3.1. Test specimens and test setup

Smooth-notched tensile coupons were extracted from steel Q235B and Q345B welded plates at the positions of base metal, weld metal and HAZ. Three notch radii *R*, 1.25, 2.50 and 5.00 mm were designed to consider different stress triaxiality conditions. The geometry of notched specimens is shown in Fig. 10, while the relative positions of specimens on the welded plate are shown in Fig. 11. Two repetitive tests were carried out for each type of coupon and the average response were used later on. A total of 36 specimens were carried out. All specimens were tested using the Zwick universal material testing machine and the whole stress-strain response was recorded until fracture. The test setup is shown in Fig. 12.
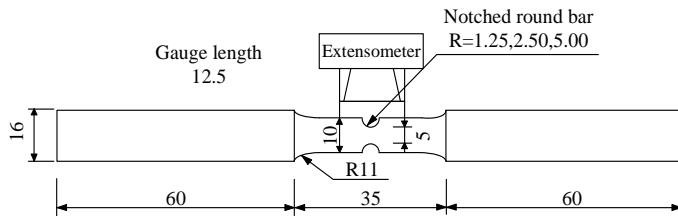

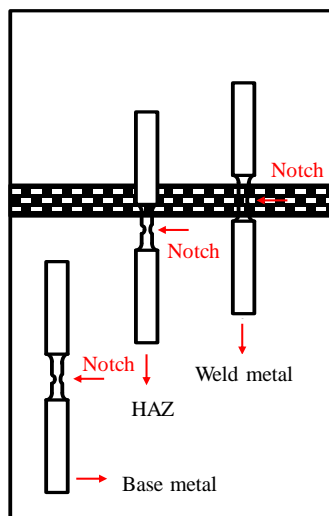**Fig. 10** Geometry of notched round bar specimen
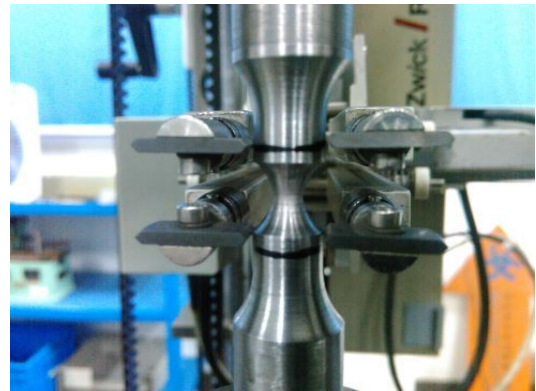

Fig. 11 Specimens layout

Fig. 12 Test setup

3.3.2. Test results

The load-displacement curves obtained from the notched bar tensile tests are shown in Fig. 13. It can be observed that all the curves have a sudden change in slope, the point with slope discontinuity is taken as the fracture initiation point. The displacement at this point was later used in the finite element analysis for the micromechanical model calibration. The obtained test results including ultimate load N_u, fracture load N_f and fracture displacement δ_f are summarised in Tables 6 and 7, for Q235B and Q345B, respectively. d_0 represents the diameter of the specimens prior to the tests. The specimens are designated with 4 letters here: the first one represents the position of the coupon (B for base metal, W for weld metal and H for heat affected zone); the second one represents the size of the notch radius in mm (S for 1.25, M for 2.50 and L for 5.00); the third letter M represents monotonic loading; the last one represents the material of the coupon (L for Q235B and H for Q345B). According to the experimental results, it can be concluded that with the increase of the notch radius of the test piece, the yield load and ultimate load of the test piece both decreases, and the displacement of the fracture increases, indicating that the larger the notch radius, the better the test piece toughness.
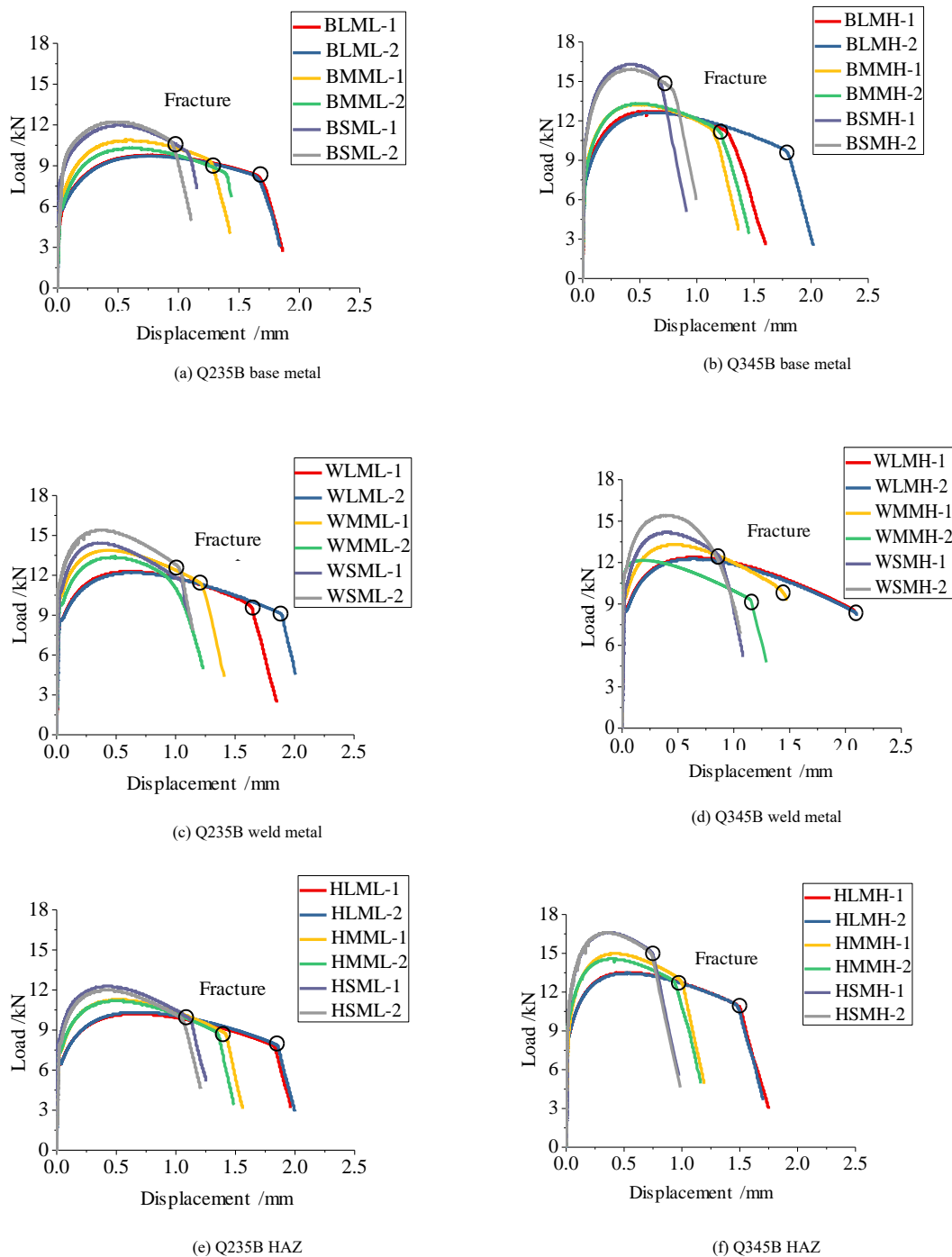
(a) Q235B base metal

(b) Q345B base metal

(c) Q235B weld metal

(d) Q345B weld metal

(e) Q235B HAZ

(f) Q345B HAZ

Fig. 13 Load-displacement curves

Table 6
Experimental results of Q235B steel

Position	R/mm	ID	d_f/d_0	δ_f / mm	N_f/kN	N_u/kN
Base metal	1.25	BSML-1	0.768	1.08	10.11	12.00
		BSML-2	0.762	0.94	10.90	12.20
	2.50	BMML-1	0.756	1.27	9.30	10.90
		BMML-2	0.759	1.40	8.36	10.30
	5.00	BLML-1	0.699	1.66	8.25	9.77
		BLML-2	0.722	1.65	8.18	9.71
Weld metal	1.25	WSML-1	0.748	1.06	11.50	14.40
		WSML-2	0.699	1.03	12.60	15.40
	2.50	WMML-1	0.694	1.22	10.30	13.40
		WMML-2	0.711	1.04	11.36	13.88
	5.00	WLML-1	0.665	1.65	9.48	12.30
		WLML-2	0.621	1.89	9.11	12.20
HAZ	1.25	HSML-1	0.735	1.13	9.75	12.30
		HSML-2	0.703	1.06	9.90	12.00
	2.50	HMML-1	0.682	1.42	8.74	11.30

		HMML-2	0.679	1.35	8.81	11.20
	5.00	HLML-1	0.667	1.83	7.78	10.20
		HLML-2	0.671	1.86	7.80	10.30

Table 7
Experimental results of Q345B steel

Position	R/mm	ID	d_f/d_0	δ_f / mm	N_f/kN	N_u/kN
Base Metal	1.25	BSMH-1	0.820	0.69	14.70	16.30
		BSMH-2	0.760	0.80	14.40	15.90
	2.50	BMMH-1	0.730	1.15	11.20	13.20
		BMMH-2	0.700	1.22	11.00	13.30
	5.00	BLMH-1	0.730	1.29	11.00	12.70
		BLMH-2	0.730	1.79	9.67	12.60
Weld metal	1.25	WSMH-1	0.756	0.89	12.10	14.20
		WSMH-2	0.787	0.90	11.50	15.40
	2.50	WMMH-1	0.563	1.15	9.24	12.20
		WMMH-2	0.548	1.42	9.98	13.30
	5.00	WLMH-1	0.578	2.08	8.53	12.40
		WLMH-2	0.601	2.10	8.32	12.30
HAZ	1.25	HSMH-1	0.769	0.75	15.00	16.60
		HSMH-2	0.770	0.75	14.80	16.60
	2.50	HMMH-1	0.730	1.00	12.80	15.00
		HMMH-2	0.740	0.94	12.80	14.60
	5.00	HLMH-1	0.674	1.50	10.90	13.50
		HLMH-2	0.685	1.48	11.00	13.50

The reduction in area was calculated from the test results. Together with the fracture displacement and ultimate load, the comparisons are summarised in Fig. 14, where the average value of each notc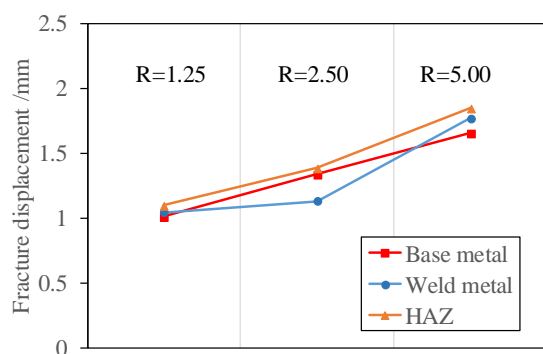h size is used. It can be seen that for most specimens the reduction in area increases with increase notch size, while the percentage reduction in area for the weld metal of Q345B is generally higher, showing better ductility.
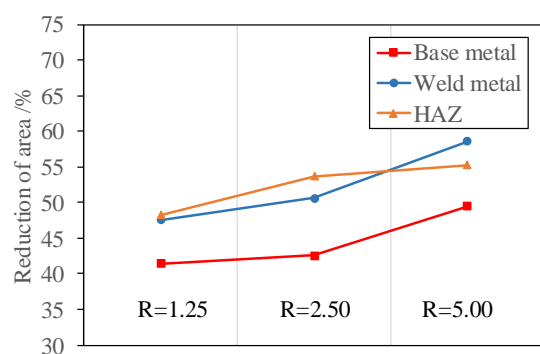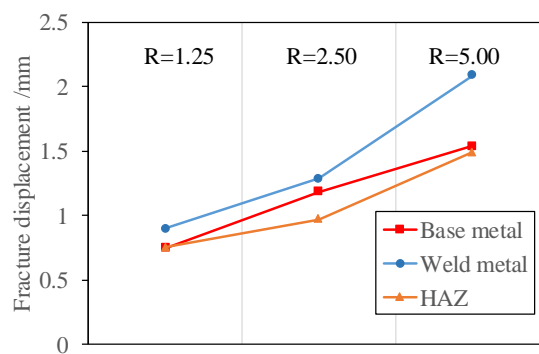

(a) Q235B reduction of area comparisons
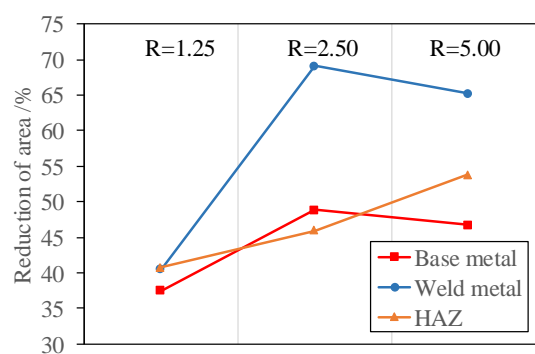
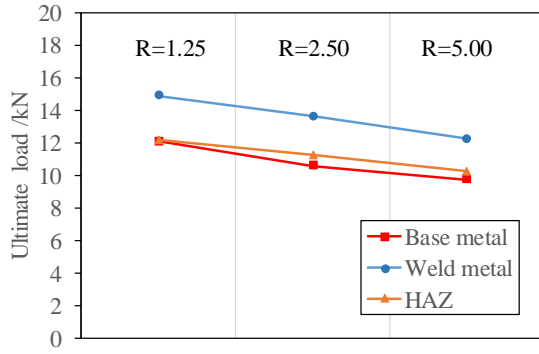

(b) Q345B reduction of area comparisons
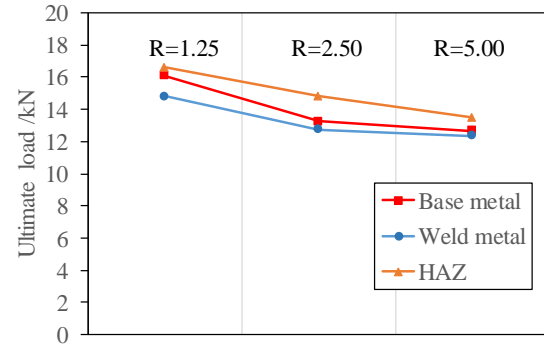

(c) Q235B displacement comparisons

(d) Q345B displacement comparisons

(e) Q235B load comparisons

(f) Q345B load comparisons

Fig. 14 Test results comparisons

According to the results of the notch round bar tensile tests in Fig. 14, it can be seen that: (1) As the radius of the notch of the round bar increases, the ultimate load decreases, while the displacement at the time of failure increases, showing the equivalent plastic strain increases with the triaxiality decreases. (2) In general, the tensile strength and plasticity of weld region for Q235B steel are higher than that of base metal, showing good welding performance. (3) Sedimentary cladding metal of Q345B steel is more plastic than the base metal, while the tensile strength is slightly lower than that of the base metal, and the tensile strength of heat affected zone is enhanced. The properties of the deposited metal are slightly different from those of the Q235 B weld. The

reason may be that the weld pool is wider. The fusion of Q345 B steel and weld seam is weaker than that of Q235 B weld. The heat affected zone of the heated edge is prone to hardening under the influence of thermal cycling.

3.3.3. Macroscopic fracture analysis

Same as in 3.3.1 scanning electron microscope (SEM) measurements were taken for all specimens. The upper and lower limits of the characteristic length l^*, a parameter of microscopic mechanism models, were obtained from the measurements.
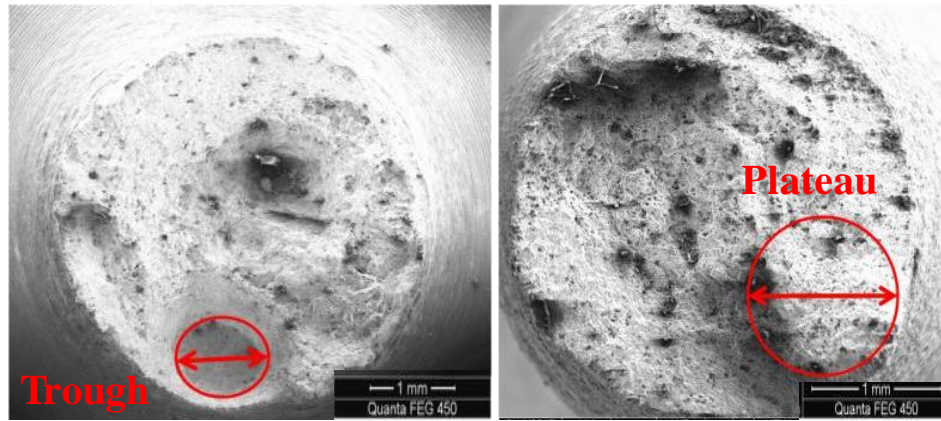
(a) Upper limit of characteristic length
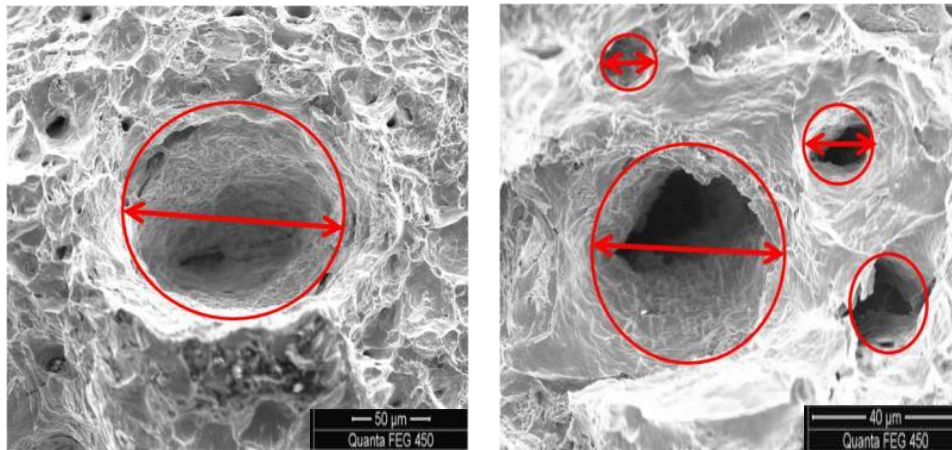
(b) Lower limit of characteristic length

Fig. 15 SEM measurements of typical fracture surfaces

Micromechanics-based model assumes crack initiation at coalescence of adjacent voids. The lower limit of the characteristic length is twice the diameter of the average dimple, while the upper limit is the size of the largest plateau or trough observed in the fractograph[23]. This method might bring scatters to the value of characteristic lengths, thus influencing the material

toughness value. The mean value of the characteristic length is taken as the average of 10 measurements of the size of plateaus or troughs. The typical fracture surfaces are shown in Fig. 15. The upper limit, average value and lower limit of the characteristic length are tabulated in Table 8.

Table 8
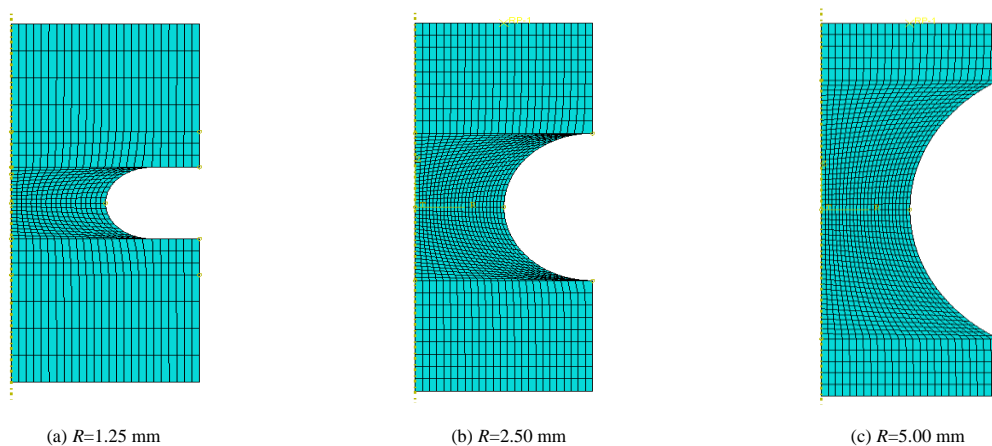Characteristic length obtained from SEM measurements (mm)

Material	ID	Characteristic length		
		Lower limit	Upper limit	Mean value
Q235B base metal	BSML-1	0.051	0.513	0.236
	BLML-2	0.075	0.886	0.230
	BMML-2	0.081	0.424	0.295
	Average	0.069	0.608	0.254
Q235B weld metal	WLML-2	0.054	0.325	0.187
	WLML-2	0.049	0.463	0.276
	WLML-2	0.035	0.428	0.228
	Average	0.046	0.405	0.230
Q235B HAZ	HSML-1	0.072	0.470	0.193
	HMML-1	0.027	0.215	0.191
	HMML-1	0.038	0.283	0.187
	Average	0.046	0.323	0.190
Q345B base metal	BLMH-2	0.041	0.804	0.590
	BMMH-1	0.034	0.585	0.160
	BSMH-2	0.052	0.753	0.482
	Average	0.042	0.714	0.411
Q345B weld metal	WSMH-2	0.068	0.385	0.297
	WMMH-2	0.042	0.519	0.222
	WLMH-1	0.075	0.397	0.174
	Average	0.062	0.434	0.231
Q345B HAZ	HMMH-1	0.045	0.502	0.148
	HLMH-2	0.047	0.452	0.241
	HSMH-1	0.036	0.428	0.122
	Average	0.043	0.461	0.17

4. Calibration and validation of micromechanical fracture models

4.1. Finite element models

Finite element models corresponding to the notched tensile test specimens were developed to calibrate the facture parameters. The general-propose finite element (FE) package ABAQUS was used. The gauge part of the specimen was simulated with axisymmetric 2-dimensional FE model with axisymmetry boundary conditions along the centre. One end of the gauge part was hinged while the other end was loaded with displacement control. The four-node axisymmetric element CAX4 from the ABAQUS element library was adopted. The geometries of the corresponding test specimens were employed, while the average material properties from the smooth round bar tensile coupon tests were used. Element size in the vicinity of the gap was taken around 0.2 mm, with reference to the aforementioned average value of characteristic length l^* obtained in the SEM measurements, as shown in Fig. 16. The fracture points obtained from the notched tensile tests, as shown in Fig. 13, were used for displacement control in the models. The load-displacement curves from the tests and FE models are compared in Figs. 17 and 18, for Q235B and Q345B respectively.
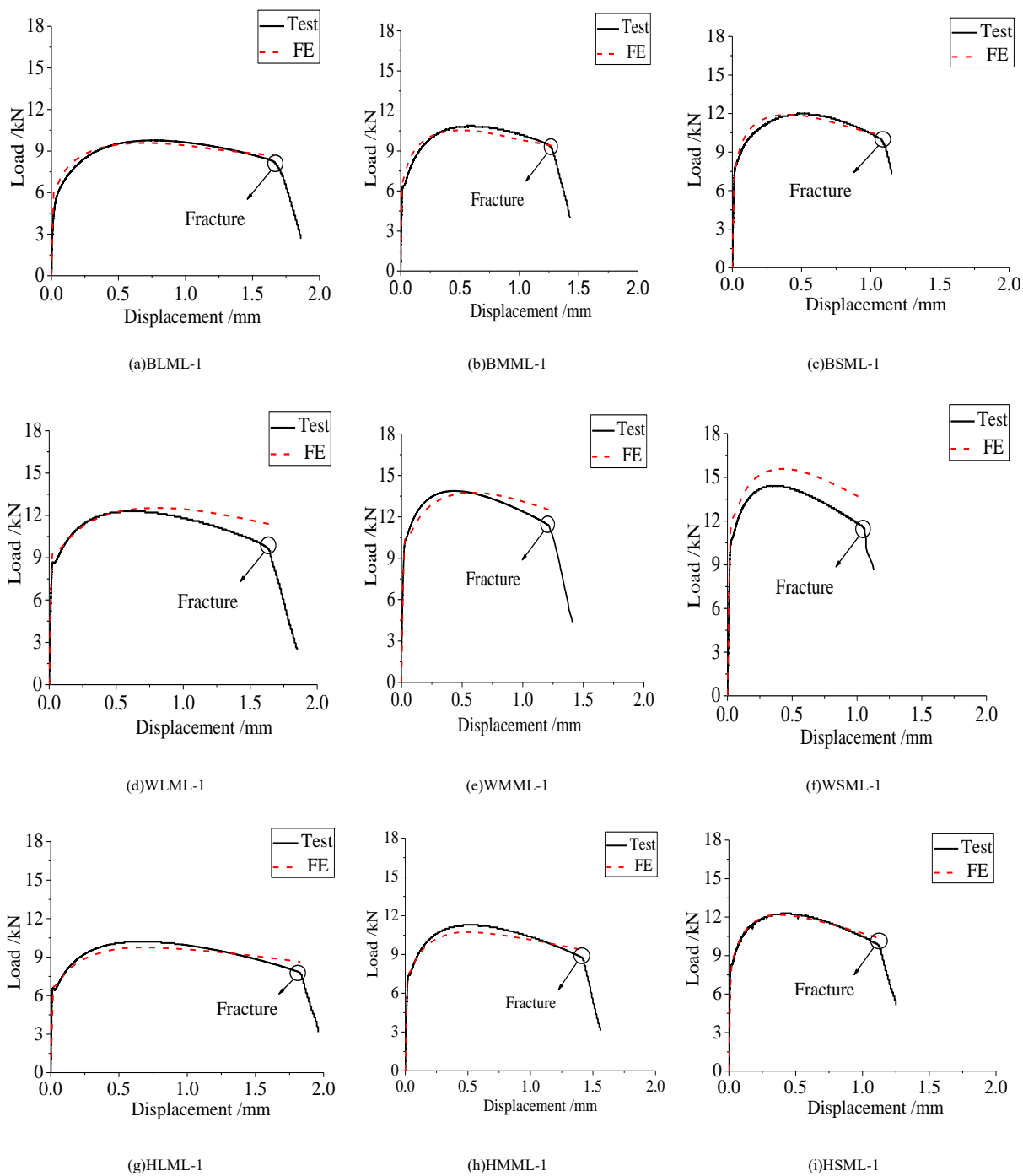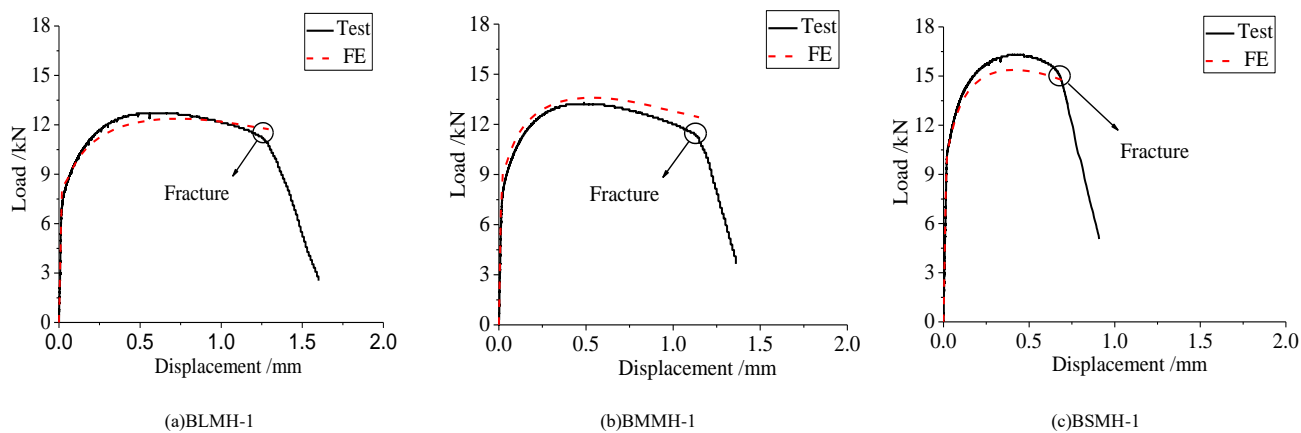

(a) *R*=1.25 mm   (b) *R*=2.50 mm   (c) *R*=5.00 mm

Fig. 16 Finite element model mesh

(a)BLML-1

(b)BMML-1

(c)BSML-1

(d)WLML-1

(e)WMML-1

(f)WSML-1

(g)HLML-1

(h)HMML-1

(i)HSML-1

Fig. 17 Load-displacement curves of Q235B

(a)BLMH-1

(b)BMMH-1

(c)BSMH-1

(c)WLMH-1

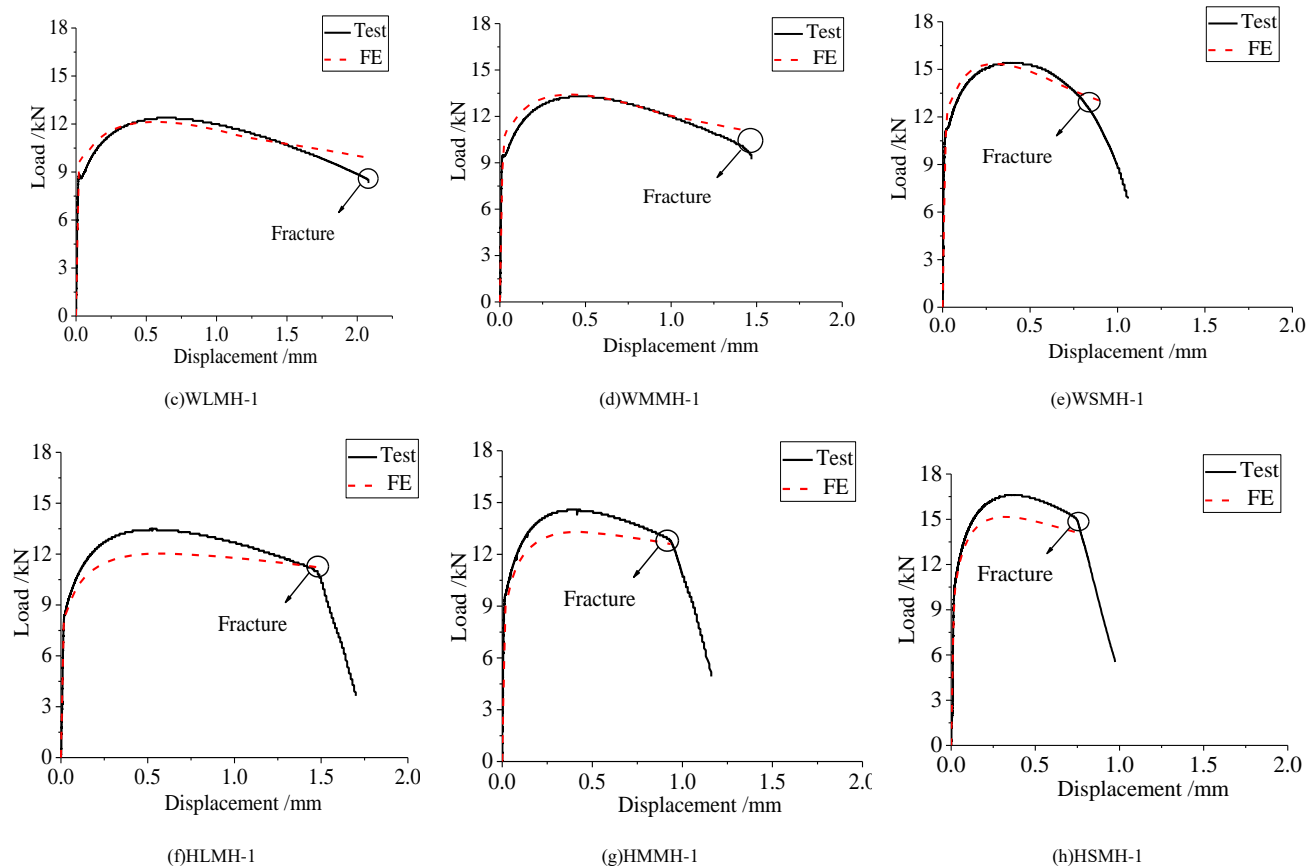(d)WMMH-1

(e)WSMH-1

(f)HLMH-1

(g)HMMH-1

(h)HSMH-1

Fig. 18 Load-displacement curves of Q345B

4.2. Toughness parameters calibration

With fracture reaching the critical state, the toughness parameters η_{mon} and γ, in VGM model and SMCS model respectively, were back-calculated through the UMAT subroutine in ABAQUS. The results at fracture displacement obtained from the finite element models are shown in Tables 9 and 10, where $\varepsilon_{p,cr}$ is plastic strain, σ_m is von Mises stress, σ_e is equivalent stress, d_f is fracture radius, T is stress triaxiality. The results show that with increasing notch radius, the stress triaxiality T decreases. It can be seen that the toughness

parameters η_{mon} and γ of Q345B are less scatter than that of the Q235B. That may be caused by the better plasticity of Q235B than that of Q345B, and the equivalent plastic strain varies greatly with the stress triaxiality, showing higher level of microvoid expansion capacity. By comparing the toughness parameters of base material, weld metal and heat affected zone, the values of heat affected zone are relative small, while the average values of these three materials are close, which indicates that the calibrated parameters can be used to predict fracture initiation in welded steel components under different stress state.

Table 9

Calibrations for toughness parameters of Q235B

Material	R/mm	ID	δ_f/mm	$\varepsilon_{p,cr}$	σ_m/MPa	d_f/d_0	σ_e/MPa	T	γ	η_{mon}
Base metal	1.25	BSML-1	1.08	0.783	680.6	0.768	768.1	0.886	2.665	2.712
		BSML-2	0.94	0.673	687.4	0.762	708.5	0.970	2.531	2.637
	2.50	BMML-1	1.27	0.637	560.2	0.756	688.8	0.813	2.094	2.311
		BMML-2	1.40	0.714	564.6	0.759	730.4	0.773	2.205	2.546
	5.00	BLML-1	1.66	0.658	473.7	0.699	699.7	0.677	1.815	1.911
		BLML-2	1.65	0.653	473.0	0.722	697.3	0.678	1.807	1.899
		Mean value							2.186	2.408
		COV							0.16	0.15
Weld metal	1.25	WSML-1	1.06	0.789	914.30	0.748	985.0	0.928	2.626	2.924
		WSML-2	1.03	0.765	908.93	0.697	971.8	0.935	2.555	2.827
	2.50	WMML-1	1.22	0.600	741.77	0.694	881.8	0.841	1.966	1.981
		WMML-2	1.04	0.503	700.47	0.711	829.5	0.844	1.631	1.648
	5.00	WLML-1	1.65	0.621	646.80	0.665	893.0	0.724	1.834	1.745
		WLML-2	1.89	0.751	714.13	0.621	967.3	0.738	2.272	2.169
		Mean value							2.147	2.216
		COV							0.19	0.25
HAZ	1.25	HSML-1	1.13	0.845	715.3	0.735	802.9	0.891	2.683	3.609
		HSML-2	1.06	0.785	707.6	0.703	775.4	0.913	2.697	3.406

	2.50	HMML-1	1.42	0.735	609.8	0.682	751.6	0.811	2.329	2.678
		HMML-2	1.35	0.691	598.3	0.679	732.0	0.817	2.274	2.548
	5.00	HLML-1	1.83	0.754	540.3	0.667	760.1	0.711	2.189	2.224
		HLML-2	1.86	0.768	545.8	0.671	766.6	0.712	2.234	2.266
		Mean value							2.401	2.789
		COV							0.10	0.21

Table 10

Calibrations for toughness parameters of Q345B

Material	R/mm	ID	δ_{f}/mm	$\varepsilon_{\mathrm{p,cr}}$	σ_{m}/MPa	d_{f}/d_0	σ_{e}/MPa	T	γ	η_{mon}
Base metal	1.25	BSMH-1	0.69	0.491	850.7	0.820	761.1	1.118	2.039	2.070
		BSMH-2	0.8	0.572	873.63	0.760	813.8	1.074	2.451	2.515
	2.50	BMMH-1	1.15	0.577	697.03	0.730	816.8	0.853	2.085	2.287
		BMMH-2	1.22	0.618	708.37	0.700	843.4	0.84	2.138	2.427
	5.00	BLMH-1	1.29	0.520	583.33	0.730	779.4	0.748	1.597	1.581
		BLMH-2	1.79	0.749	623.7	0.730	929.2	0.671	2.049	2.236
		Mean value							2.060	2.186
		COV							0.13	0.15
Weld metal	1.25	WSMH-1	0.894	0.685	875.8	0.756	827.2	1.059	3.056	3.445
		WSMH-2	0.895	0.686	875.67	0.787	827.7	1.058	3.057	3.309
	2.50	WMMH-1	1.152	0.600	714.67	0.563	780.3	0.916	2.343	2.520
		WMMH-2	1.42	0.768	732.1	0.548	871.3	0.83	2.671	3.105
	5.00	WLMH-1	2.079	0.944	698.97	0.578	965.4	0.724	2.796	2.919
		WLMH-2	2.100	0.955	703.87	0.601	971.3	0.725	2.831	2.951
		Mean value							2.792	3.042
		COV							0.10	0.11
HAZ	1.25	HSMH-1	0.748	0.522	924.87	0.769	828.6	1.116	2.263	2.298
		HSMH-2	0.745	0.520	924.27	0.770	827.3	1.117	2.251	2.284
	2.50	HMMH-1	1.000	0.483	751.13	0.730	805.8	0.932	1.913	1.938
		HMMH-2	0.936	0.447	748.1	0.740	785.1	0.953	1.812	1.785
	5.00	HLMH-1	1.500	0.62	648.33	0.674	884.3	0.733	1.860	1.898
		HLMH-2	1.480	0.61	645.47	0.685	878.8	0.734	1.836	1.869
		Mean value							1.989	2.012
		COV							0.11	0.11

4.3. Discussions

Having calibrated the toughness parameters of the two models, numerical results were compared and discussed.

The von Mises stress field, triaxiality stress field and the equivalent plastic strain field of a typical group of specimens (Q345B base metal specimens with different notch sizes) are shown in Fig. 19. Specimens with different notch sizes shows different stress and strain fields.
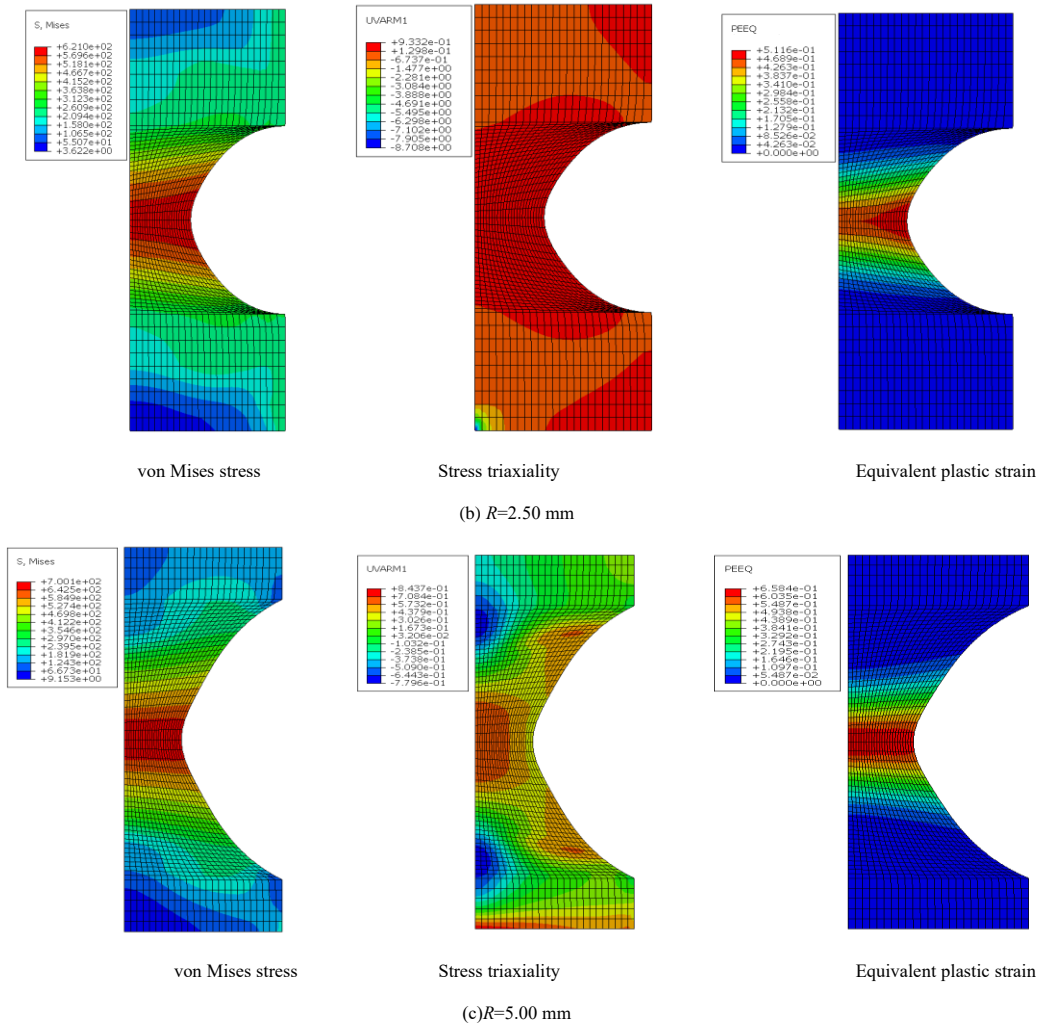

von Mises stress   Stress triaxiality   Equivalent plastic strain

(a) *R*=1.25 mm

von Mises stress   Stress triaxiality   Equivalent plastic strain

(b) *R*=2.50 mm

von Mises stress   Stress triaxiality   Equivalent plastic strain

(c)*R*=5.00 mm
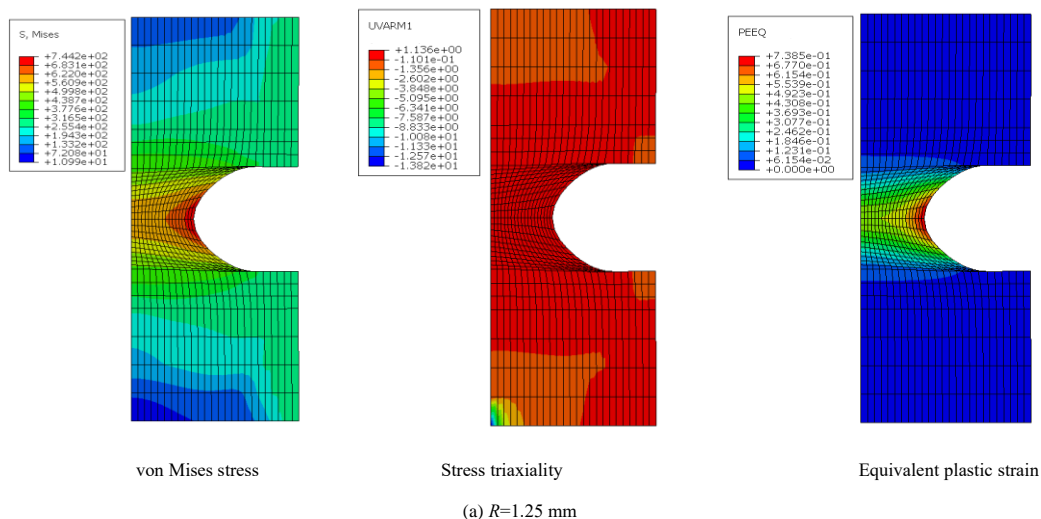
Fig. 19 Distribution of stress and strain fields in notched area

The equivalent plastic strain and triaxial stress distribution along the notched cross-section at crack initiation is shown in Figs. 20 and 21, respectively. PEEQ is the value of equivalent plastic strain while UVARM1 is the stress triaxiality, output from the subroutine in ABAQUA. It can be observed that for round bars with a notch radius of *R*=5.00 mm, the equivalent plastic strain is distributed uniformly along the notched section. With smaller notch radius of *R*=2.50 mm and 1.25 mm, the equivalent plastic strain is high at the edge and low near the centre. The maximum UVARM1 value, namely stress triaxiality, appears at the centre of the test piece, unlike the equivalent plastic strain distribution. Therefore, the fracture of materials, especially those in triaxial stress state, cannot be predicted with only equivalent plastic strain. The micromechanical fracture models take into consideration of the influence of both stress triaxiality and equivalent plastic strain, thus giving better predictions.
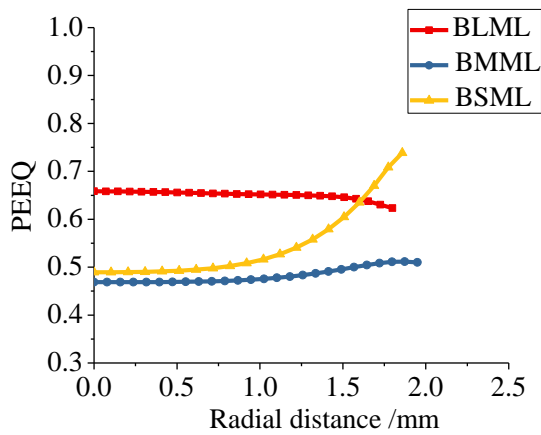
(a) Q235B base metal
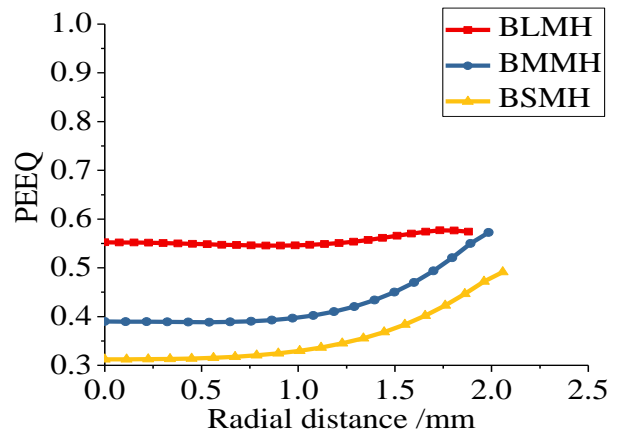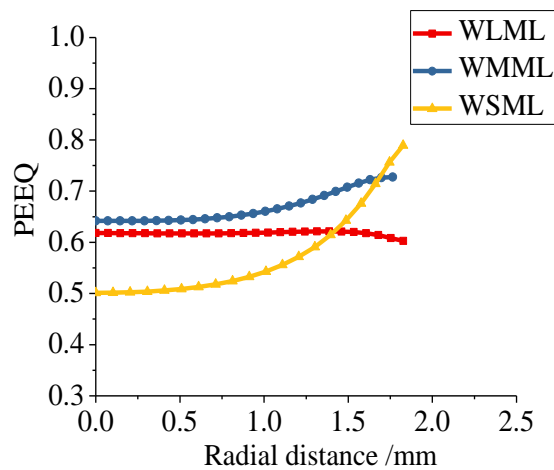
(b) Q345B base metal
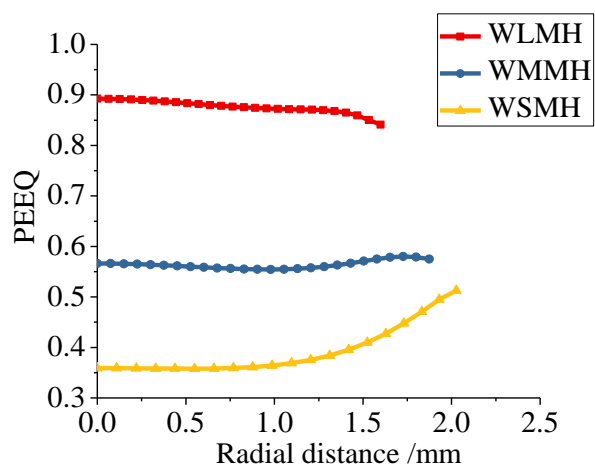
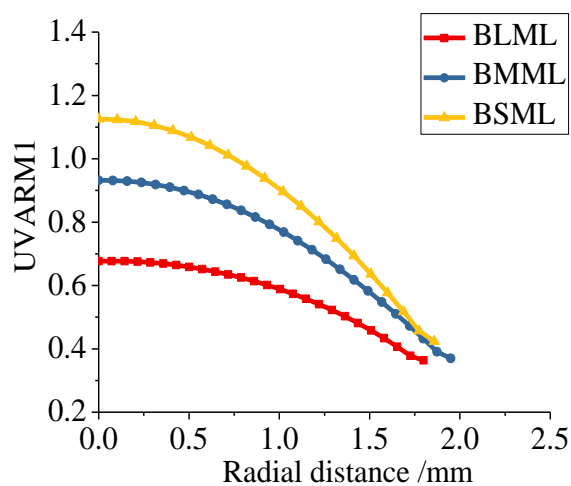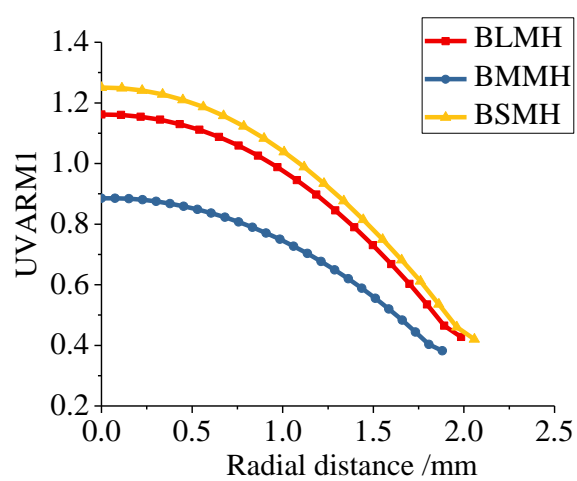(c) Q235B weld metal

(d) Q345B weld metal
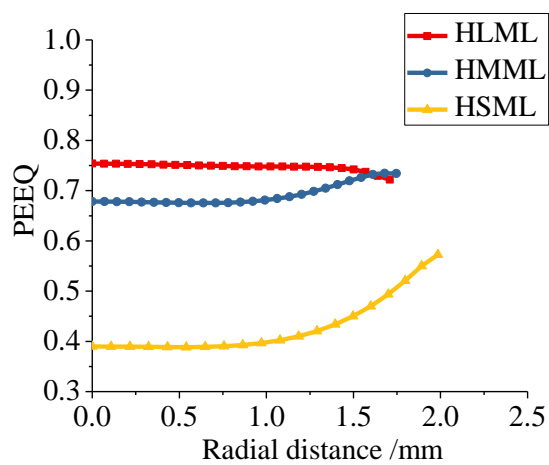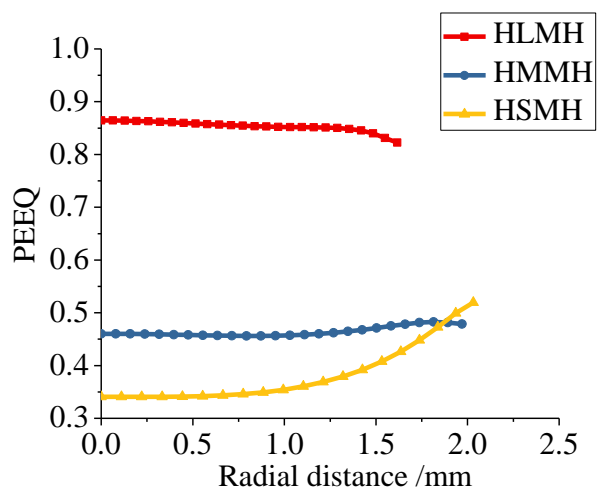
(e) Q235B HAZ

(f) Q345B HAZ

Fig. 20 Equivalent plastic strain of Q235B and Q345B

(a) Q235B base metal

(b) Q345B base metal

(c) Q235B weld metal

(d) Q345B weld metal
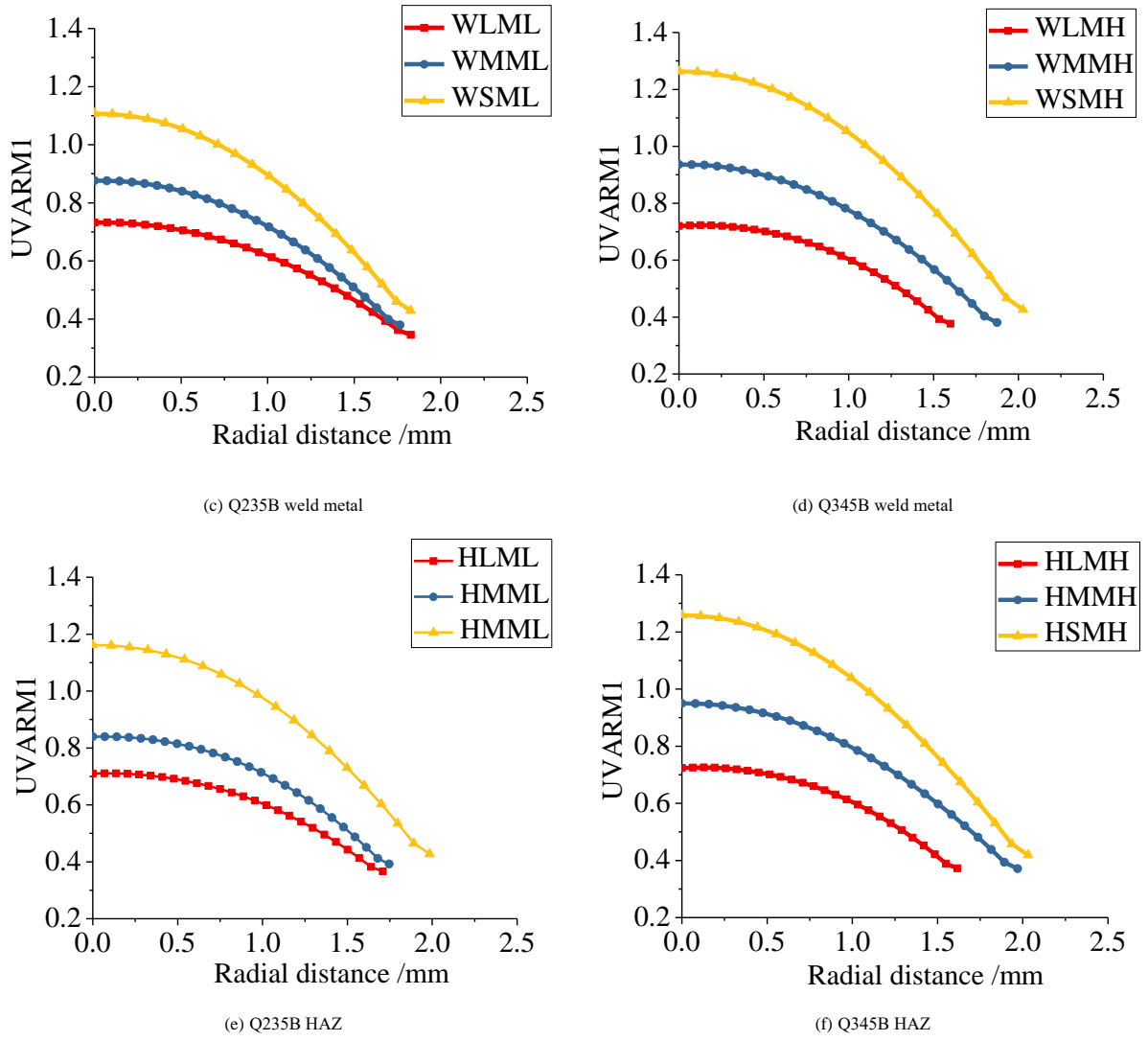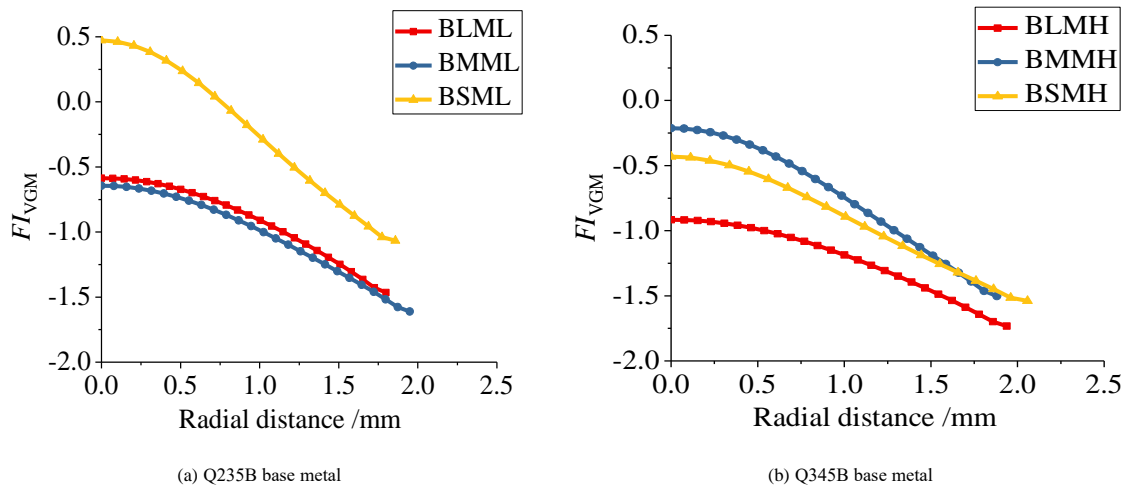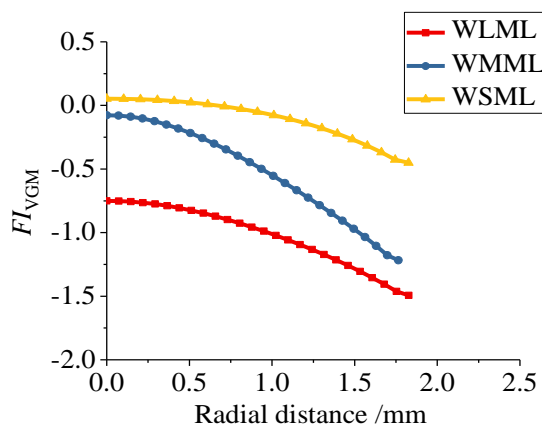

(e) Q235B HAZ

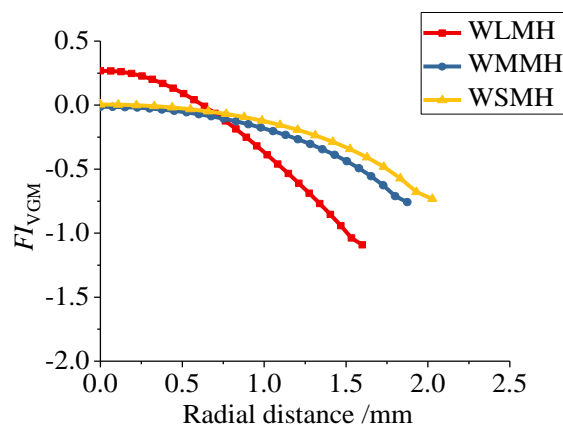(f) Q345B HAZ

Fig. 21 UVARM1 of Q235B and Q345B

Figs. 22 and 23 show the VGM and SMCS fracture index, FI_{VGM} and FI_{SMCS} respectively, distribution along the notched cross-section at the fracture initiation (when fracture displacement is reached in the numerical model). It can be seen that the fracture index is biggest at the centre of the bar, indicating that the fracture initiates from the centre. This is consistent with the observations from the SEM measurements. For the three different stress states, the fracture parameters of the SMCS model and the VGM model show similar distributions along the notched cross-section: decreasing from the centre to the edge, having less change within a certain range. This also shows that for the notched round bar specimen, the value of the characteristic length based on the microstructure of the material has little effect on the fracture prediction, and there is no obvious correlation between the characteristic length and the value of the toughness parameters. The consistency in the distribution of fracture parameters in VGM and SMCS also shows that both models offer similar predictions under different stress states.
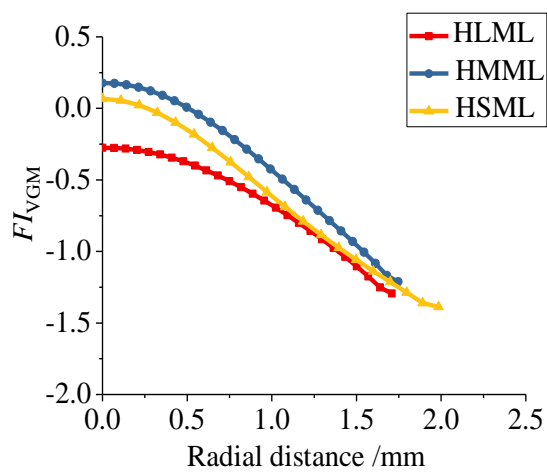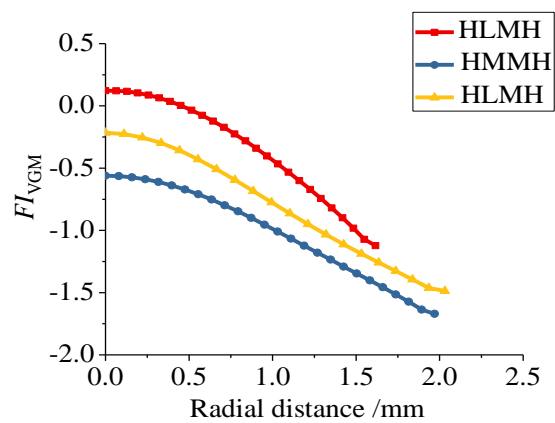

(a) Q235B base metal

(b) Q345B base metal

(c) Q235B weld metal
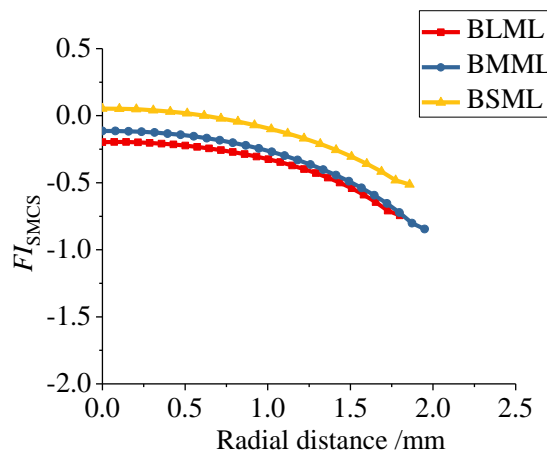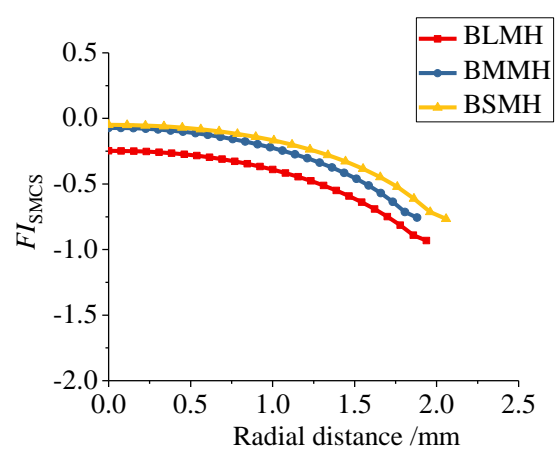

(d) Q345B weld metal

(e) Q235B HAZ

(f) Q235B HAZ

Fig. 22 Distribution of SMCS fracture index

(a)Q235B base metal
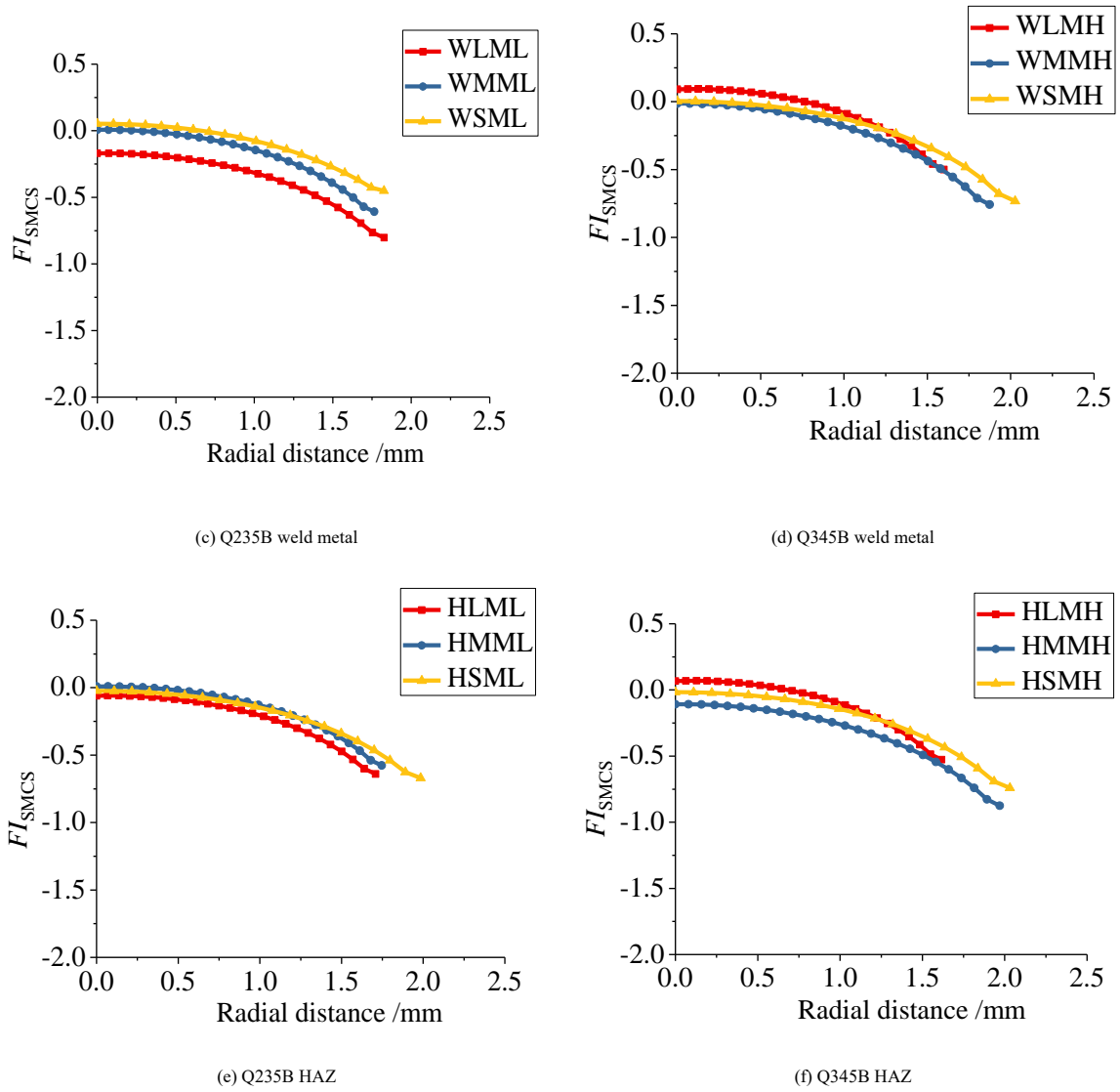

(b)Q345B base metal

(c) Q235B weld metal


(d) Q345B weld metal

(e) Q235B HAZ

(f) Q345B HAZ

Fig. 23 Distribution of SMCS fracture index

4.4. Fracture prediction

With the calibrated toughness parameters, as listed in Tables 9 and 10, the load-displacement response of monotonic experiments can be predicted with the VUMAT subroutine in ABAQUS. The comparisons of load-displacement curves are shown in Figs. 24 to 26. Note that the FE curves are without

subroutine and displacement controlled till the fracture displacement obtained in the tests. The fracture load and displacement obtained by tests are compared with the predictions in Tables 11 and 12, respectively. The fracture load and displacement predictions are compared with test results in Figs. 27 and 28, respectively. The typical test curves from each set of two repetitive specimens were employed.
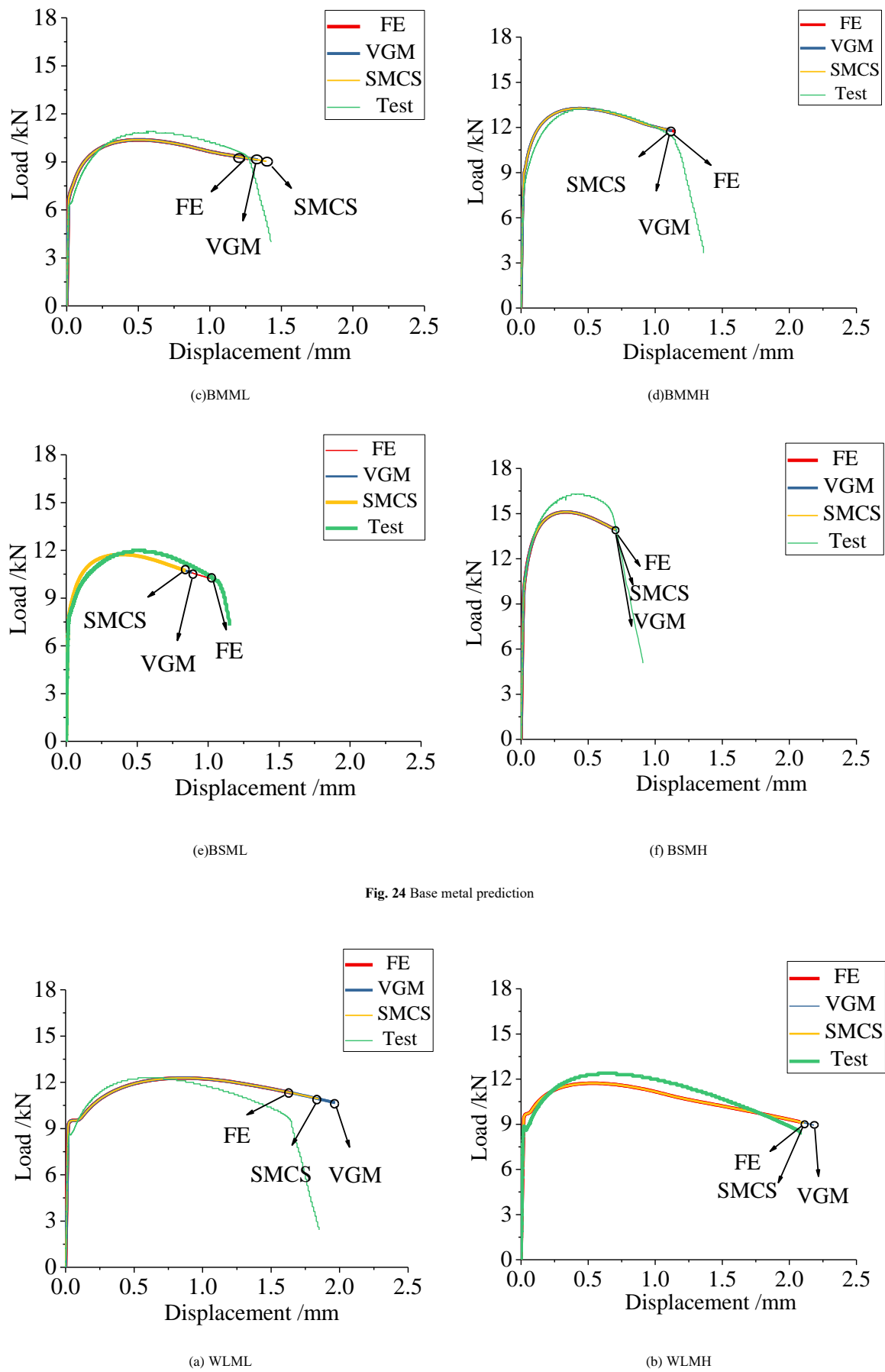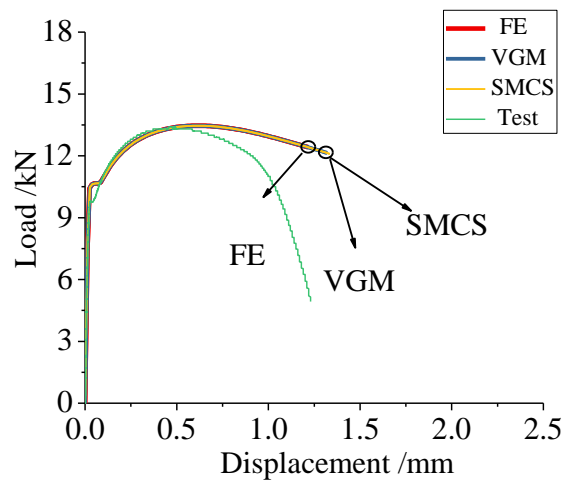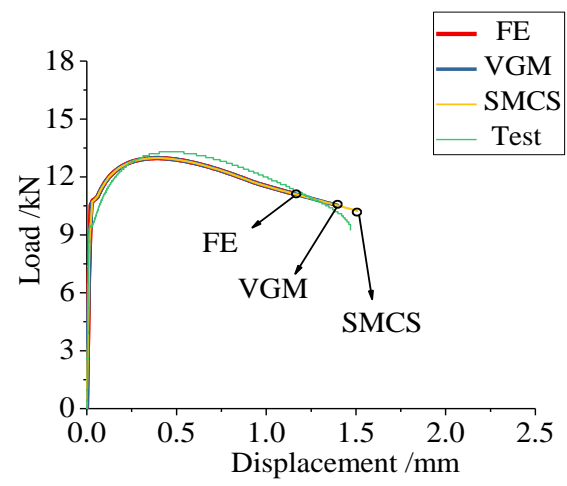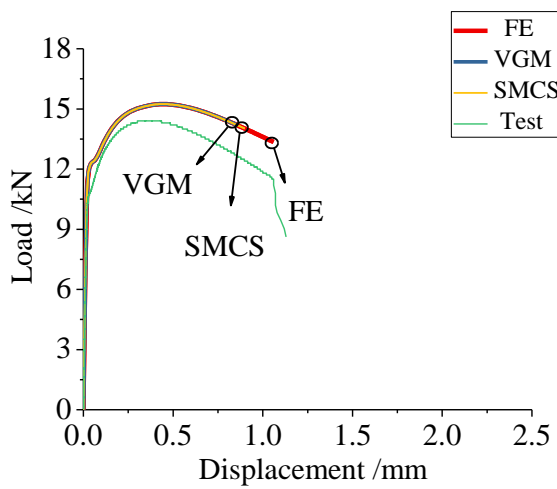

(a)BLML

(b)BLMH

(c)BMML

(d)BMMH

(e)BSML

(f) BSMH
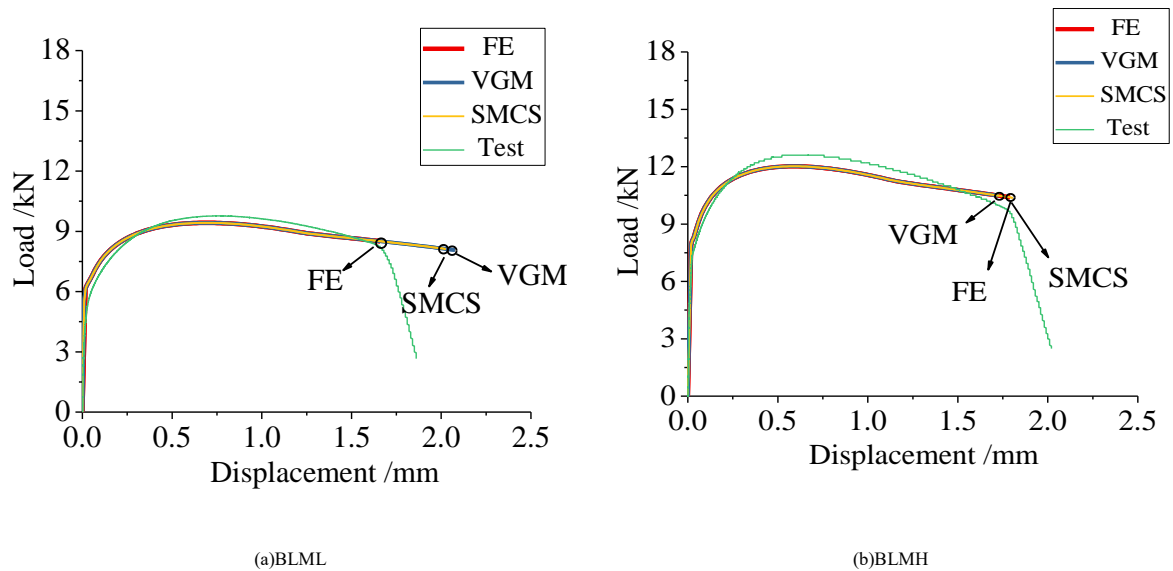
Fig. 24 Base metal prediction

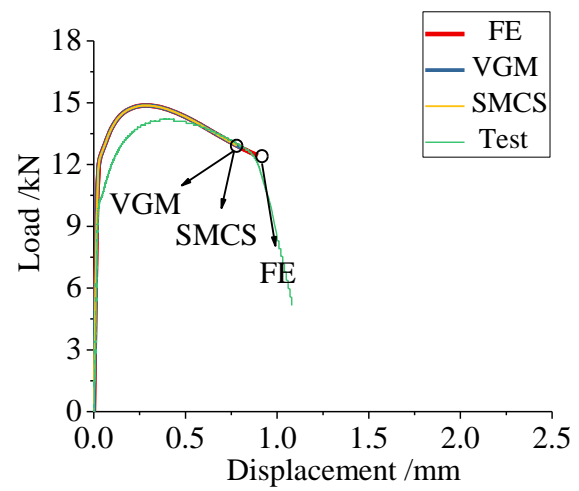

(a) WLML

(b) WLMH

(c) WMML

(d) WMMH

(e) WSML

(f) WSMH

Fig. 25 Weld metal prediction

(a) HLML

(b) HLMH

(c) HMML
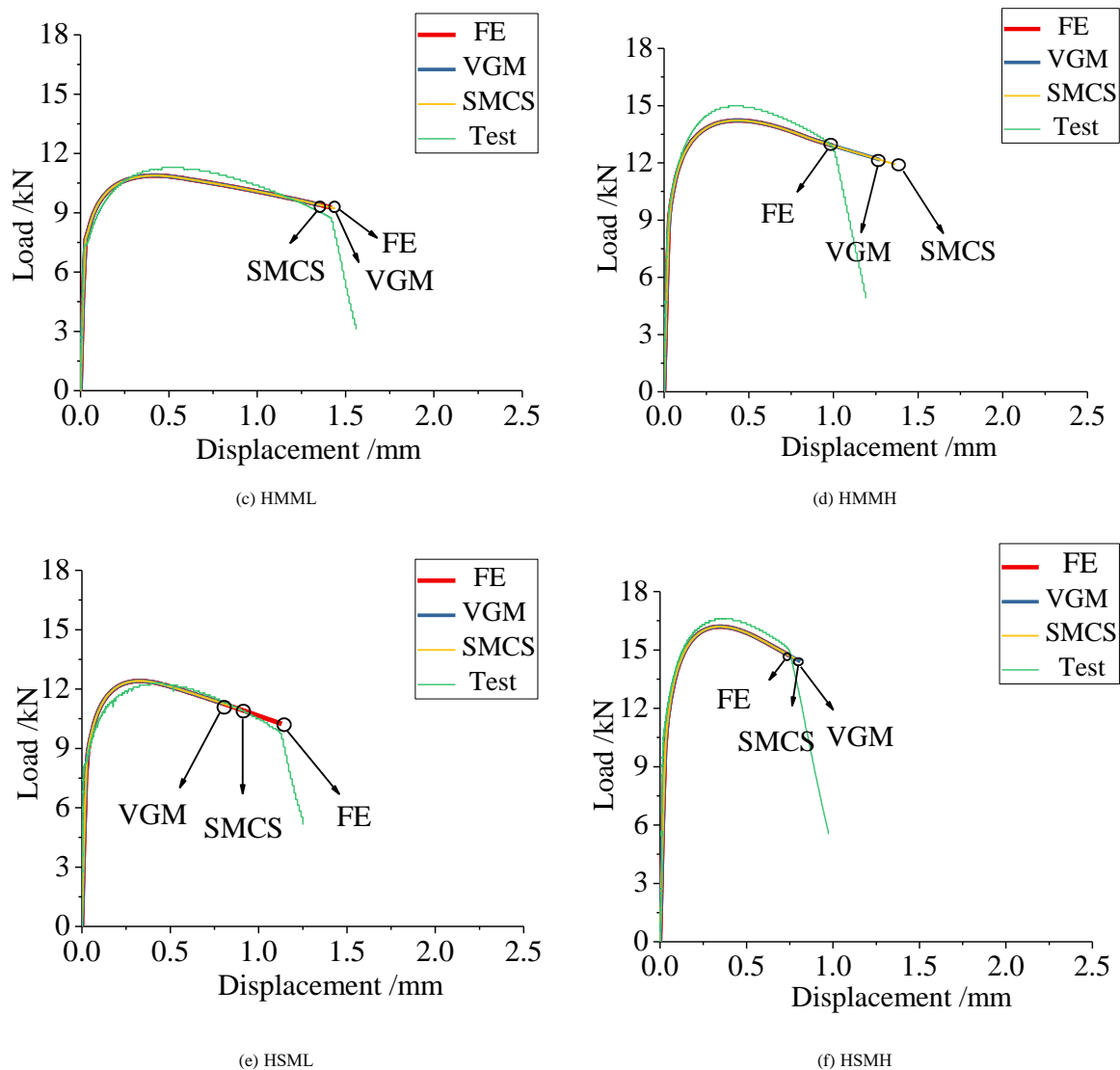

(d) HMMH

(e) HSML
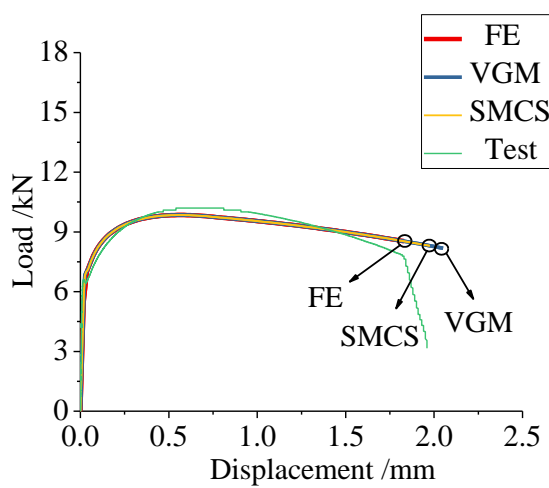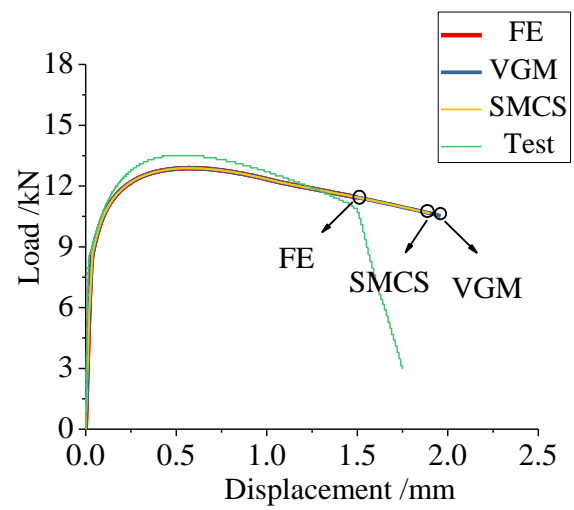
(f) HSMH

Fig. 26 HAZ prediction

Table 11
Fracture load comparisons (kN)

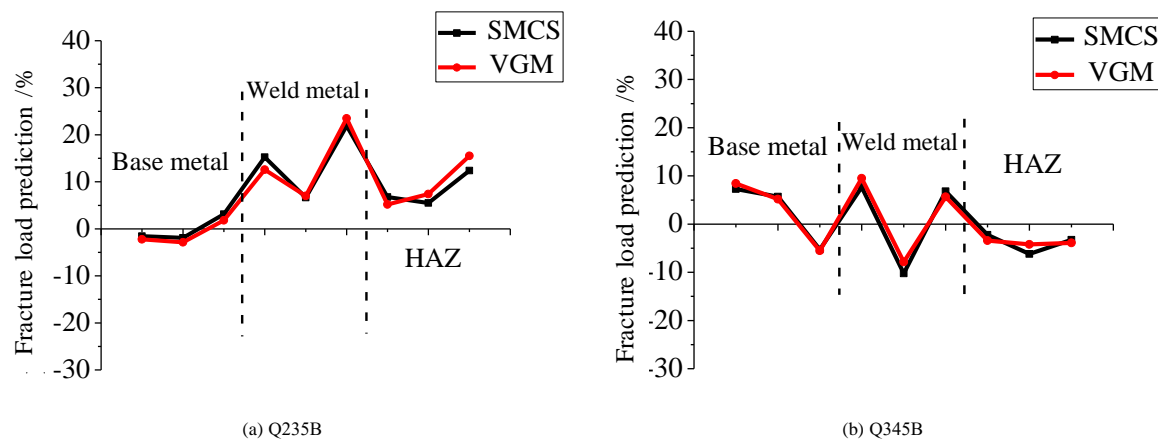| Specimen ID	Test	SMCS Prediction	(SMCS-Test)/Test%	VGM Prediction	(VGM-Test)/Test%
BLMH	9670	10373.70	7.28	10486.60	8.44
BLML	8250	8123.20	-1.54	8064.87	-2.24
BMMH	11200	11838.10	5.70	11778.70	5.17
BMML	9300	9123.40	-1.90	9032.93	-2.87
BSMH	14700	13924.50	-5.28	13888.10	-5.52
BSML	10400	10724.50	3.12	10590.50	1.83
WLMH	8310	8946.89	7.66	9100.04	9.51
WLML	9480	10926.50	15.26	10672.60	12.58
WMMH	11400	10231.10	-10.25	10504.80	-7.85
WMML	11344	12096.50	6.64	12137.90	7.00
WSMH	12100	12925.20	6.82	12785.00	5.66
WSML	11500	14019.80	21.91	14200.60	23.48
HLMH	10900	10655.30	-2.24	10527.90	-3.41
HLML	7780	8305.35	6.75	8182.78	5.18
HMMH	12700	11914.70	-6.18	12163.00	-4.23
HMML	8740	9219.70	5.49	9385.77	7.39
HSMH	15000	14510.90	-3.26	14417.50	-3.88
HSML	9750	10957.40	12.38	11262.40	15.51

(a) Q235B   (b) Q345B

Fig. 27 Fracture load prediction

Table 12
Fracture displacement comparisons (mm)

| Specimen ID	Test	VGM displacement of prediction	(VGM-Test)/Test%	SMCS displacement of prediction	(SMCS-Test)/Test%
BLMH	1.790	1.726	-3.60	1.806	0.89
BLML	1.660	2.076	25.06	2.026	22.05
BMMH	1.150	1.125	-2.17	1.095	-4.78
BMML	1.270	1.335	5.12	1.395	9.84
BSMH	0.691	0.712	3.04	0.704	1.88
BSML	1.020	0.885	-13.24	0.840	-17.65
WLMH	2.079	2.182	4.95	2.107	1.35
WLML	1.650	1.966	19.15	1.846	11.88
WMMH	1.152	1.404	21.88	1.512	31.25
WMML	1.216	1.320	8.55	1.335	9.77
WSMH	0.894	0.810	-23.38	0.780	-12.75
WSML	1.060	0.855	-19.34	0.900	-15.09
HLMH	1.500	1.960	30.67	1.900	26.67
HLML	1.830	2.051	12.08	1.976	8.00
HMMH	1.000	1.275	27.50	1.365	36.50
HMML	1.420	1.360	-4.23	1.440	1.41
HSMH-1	0.748	0.81	8.29	0.790	5.61
HSML-1	1.130	0.80	-29.20	0.900	-20.35

(a) Q235B   (b) Q345B
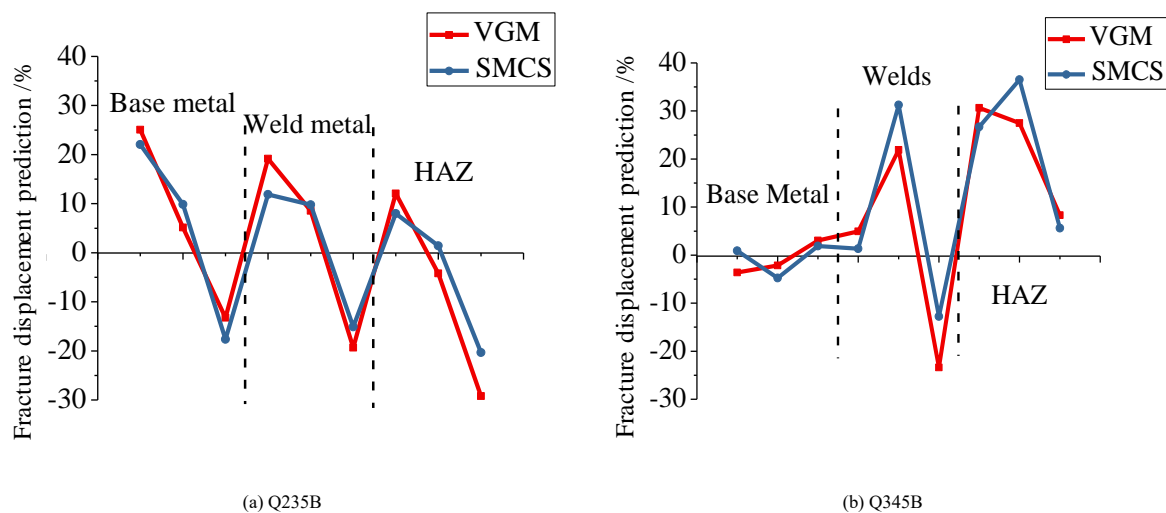
Fig. 28 Fracture displacement prediction

From Fig. 27, it can be seen that both VGM and SMCS model offer good predictions of the failure loads for Q235B and Q345B, especially for the base metal. While the predictions of the weld metal and heat affected zone are more scattered, which might be attributed to the welding effect. Fig. 28 shows that both models offer the fracture displacement prediction within 25% for base metal, yet the weld metal and HAZ reveals larger level of scatter. In general, VGM model and SMCS model are shown to be applicable to predict the ductile fracture of ordinary steel under different stress states, while for welding seam and HAZ scatter should be expected.

5. Conclusions

In this paper 12 smooth round bars and 36 notched round bars were tested under axial tensile load. The fracture behaviour of the base material, the weld metal and the HAZ of welded structural steels Q235B and Q345B were investigated. Two micromechanical fracture models: void growth model (VGM) and stress modified critical strain model (SMCS) were investigated.

The material toughness parameters η_{mon} and γ of micromechanical fracture models VGM and SMCS for each material, including the base material, the weld metal and the HAZ of Q235B and Q345B structure steel were calibrated by the tests results. Finite element analysis integrated with the micromechanical models were carried out to simulate the fracture behaviour of these tested specimens. Fracture index distributions show that the fracture initiated from the centre of the specimens, which coincides with the SEM measurements. Upon calibrations, the two models were used to predict the fracture load and displacement and the predictions were compared with the test results. The comparisons show that VGM model and SMCS model offer accurate ductile fracture prediction for the base metal under different stress states, while for welding seam and HAZ scatter should be expected.

Compliance with Ethical Standards:

Conflict of interest: The authors declared that they have no conflicts of interest to this work.

Reference

[1] F. A. McClintock, A criterion for ductile fracture by the growth of holes. Journal of Applied Mechanics. 35 (2) (1968) 363-371.

[2] J. R. Rice, D. M. Tracey, On the ductile enlargement of voids in triaxial stress fields. Journal of Mechanics and Physics of Solids. 17 (3) (1969) 201-217.

[3] J. W. Hancock, A. C. Mackenzie, On the mechanics of ductile failure in high-strength steel subjected to multi-axial stress states. Journal of the Mechanis and of Physics of Solids. 24 (3) (1976) 147-169.

[4] J. W. Hancock, M. J. Cowling, Role of state of stress in crack-tip failure processes, Metal Science. 14 (8-9) (1980) 293-304.

[5] J. W. Hancock, D. K. Brown, On the role of strain and stress state in ductile failure. Journal of the Mechanics & Physics of Solids, 31 (1) (1983) 1-24.

[6] G. R. Johnson, W. H. Cook, A constitutive model and data for metals subjected to large strains, high strain rates and high temperatures. Proceedings of the 7th International Symposium on Ballistics, The Hague. (1983) 541-547.

[7] B. Marini, F. Mudry, A. Pineau. Ductile rupture of A508 steel under nonradial loading. Engineering Fracture Mechanics. 22 (3) (1985) 375-386.

[8] T. L. Panontin, S. D. Sheppard. The relationship between constraint and ductile fracture initiation as defined by micromechanical analyses, Fracture Mechanics. (1995), 54-85.

[9] J. P. Bandstra, D. A. Koss. A simulation of growth and coalescence of voids during ductile fracture. Materials Science & Engineering A. 387 (1) (2004) 399-403.

[10] A. M. Kanvinde, G. G. Deierlein. Void growth model and stress modified critical strain model to predict ductile fracture in structural steels. Journal of Structural Engineering. 132 (12) (2006) 1907-1918.

[11] W. M. Chi, A. M. Kanvinde, G. G. Deierlein, Prediction of ductile fracture in steel connections using SMCS criterion. Journal of Structural Engineering. 132 (2) (2006) 171-181.

[12] A. A. Benzerga, Micromechanical Models of Ductile Damage and Fracture. Springer New York. (2015) 939-962.

[13] A. T. Myers, G. G. Deierlein, A. M. Kanvinde, Testing and probabilistic simulation of ductile fracture initiation in structural steel components and weldments. Report No.170, the John A.Blume Earthquake Engineering Center, Stanford University, CA, 2009.

[14] Y. Q. Wang, H. Zhou, Y. J. Shi, J. Xiong, Fracture prediction of welded steel connections using traditional fracture mechanics and fracture mechanics and calibrated fracture mechanics and calibrated micromechanics-based model．International Journal of Steel Structures. 11 (3) (2011) 351-366.

[15] P. G. Kossakowski, Prediction of ductile fracture for S235JR steel using the stress modified critical strain and Gurson-Tvergaard-Needleman models. Journal of Materials in Civil Engineer. 24 (12) (2012) 1492-1500.

[16] F. F. Liao. Criterion of micro-cracking criterion of steel and its application in prediction of ductile fractures at nodes (in Chinese)..Shanghai, Tongji University, 2012.

[17] R. Kiran, K, Khandelwal, Experimental studies and models for ductile fracture in ASTM A992 steels at high triaxiality. Journal of Structural Engineering, ASCE. 140 (2) (2013) 1-48.

[18] X. Y. Liu, Study on fracture property of high strength steel structure materials and joints based on microscopic mechanism. Beijing, Tsinghua University, 2015.

[19] L. Lu, Experiment and analysis of ductile fracture of steel based on microscopic mechanism.

Nanjing, Southeast University, 2015.

[20] GB/T 228.1-2010. Metallic materials-Tensile testing -Part 1: Method of test at room temperature (in Chinese). Beijing: Standards Press of China, 2010.

[21] B. Xiao, L. Xu, L. Zhao, H. Jing, Y. Han, Z. Tang, Microstructure evolution and fracture mechanism of a novel 9Cr tempered martensite ferritic steel during short-term creep. Materials Science and Engineering. A. (2017) 466-477.

[22] A. M. Kanvinde, G. G. Deierlein, Micromechanical simulation of earthquake-induced fracture in steel structures. Report No.145, the John A. Blume Earthquake Engineering Center, Stanford University, CA, 2004.